

SURFACE PASSIVATION FOR ENHANCED STABILITY AND PERFORMANCE IN PEROVSKITE SOLAR CELLS

A Dissertation
Presented to
The Academic Faculty

by

Sakshi Sharma

In Partial Fulfillment
of the Requirements for the Degree
Master of Science in the
School of Materials Science and Engineering

Georgia Institute of Technology
December 2023

COPYRIGHT © 2023 BY SAKSHI SHARMA

SURFACE PASSIVATION FOR ENHANCED STABILITY AND PERFORMANCE IN PEROVSKITE SOLAR CELLS

Approved by:

Dr. Juan-Pablo Correa-Baena, Advisor
School of Materials Science and Engineering
Georgia Institute of Technology

Dr. Antonio Facchetti
School of Materials Science and Engineering
Georgia Institute of Technology

Dr. Faisal Alamgir
School of Materials Science and Engineering
Georgia Institute of Technology

Date Approved: December 06, 2023

ACKNOWLEDGEMENTS

To begin, I would like to acknowledge my advisor, Dr. Juan Pablo Correa- Baena for his trust and confidence in me right from the time I started my master's. Thanks to Juan Pablo's immense support and guidance, I have grown as a researcher. I would like to extend a special thanks to Dr. Carlo Perini, my first mentor in graduate school who introduced me to the world of perovskites, trained me, and spent countless hours on scientific discussions during my degree. Your mentorship enriched my experience, making this work what it is. I also thank my peers at the Energy Materials Lab for feedback and encouragement, helping me build my knowledge.

This work has been made possible through invaluable collaboration with a great number of people. I would like to thank Sarah Wieghold and Naveed Rahman for their assistance with XBIC and XEOL measurements and processing, a significant part of this work. Additionally, I would like to acknowledge Sarah for her tremendous help with KPFM measurements and analysis. I extend my acknowledgement to Dr. Ruipeng Li for carrying out the GIWAXS measurements that formed a big part of answering the questions in this thesis. I would like to thank Dr. Guoxiang Hu and Courtney Brea for undertaking DFT computations, which helped me strengthen the discussions in this thesis. I would also like to thank the members of my committee, Dr. Antonio Facchetti and Dr. Faisal Alamgir, for giving me the opportunity to present, and enhance this work. I would like to especially thank my mother and father, and my brother, who have provided me with company and comfort from across the world. I extend my gratitude to all my friends for always supporting me. Finally, thank you to Arturo, for navigating the highs and lows of my graduate school journey with me.

TABLE OF CONTENTS

ACKNOWLEDGEMENTS	iii
LIST OF TABLES	vi
LIST OF FIGURES	vii
LIST OF SYMBOLS AND ABBREVIATIONS	x
SUMMARY	xiii
Chapter 1. INTRODUCTION	1
1.1 Growing Energy Demand	1
1.2 Evolution of Photovoltaic technology	4
1.3 Perovskite Solar Cells- An overview.....	6
1.4 Aim of this thesis	8
Chapter 2. BACKGROUND	10
2.1 Properties of Lead Halide Perovskites	10
2.1.1 Crystal Structure and Optoelectronic Properties	10
2.1.2 Perovskite Dimensionality.....	14
2.1.3 Perovskite Solar Cell Fabrication	16
2.2 Perovskite degradation mechanisms and stability approaches.....	20
2.2.1 Stability under heat.....	20
2.2.2 Stability in air	23
2.2.3 Interfacial Engineering in Perovskite solar cells	23
Chapter 3. EXPERIMENTAL METHODS	29
3.1 Perovskite Solar Cell and Thin Film Fabrication	29
3.2 Compositional and Structural Characterizations on Films	30
3.2.1 X-ray Photoelectron Spectroscopy	30
3.2.2 Scanning Electron Microscopy.....	31
3.2.3 Grazing Incidence Wide Angle X-ray Scattering.....	32
3.3 Optical Characterizations	33
3.3.1 X-ray excited optical luminescence.....	33
3.4 Electrical Characterization	34

3.4.1 X-ray beam induced current	34
3.4.2 Kelvin Probe Force Microscopy	35
3.4.3 Current Density-Voltage Characteristics (J-V)	38
Chapter 4. STERIC ENGINEERING CONTROLLED STABILITY OF CSFAPBI₃ INTERFACES.....	39
4.1 Introduction.....	39
4.2 Results and Discussion.....	40
4.2.1 Surface morphology change	40
4.2.2 Surface chemistry change.....	41
4.2.3 Surface versus bulk crystal structure	43
4.2.4 DFT Simulation of cation binding energy	45
4.3 Conclusion.....	46
Chapter 5. INFLUENCE OF CAPPING LAYER ON CHARGE EXTRACTION IN PEROVSKITE SOLAR CELLS	48
5.1 Introduction.....	48
5.2 Device Performance	49
5.2.1 Surface Photovoltage.....	49
5.2.2 Charge carrier dynamics.....	51
5.2.3 J-V characteristics.....	53
5.3 Mechanism and Conclusion	57
Chapter 6. CONCLUSIONS AND OUTLOOK.....	60
6.1 Summary	60
6.2 Future Work	61
APPENDIX. Supporting Information.....	63
Perovskite film fabrication	63
Film Morphology.....	64
Surface Composition Analysis	65
Surface Structure Analysis.....	67
KPFM Surface potential distribution.....	69
REFERENCES.....	72

LIST OF TABLES

Table 1. Examples of perovskite structures based on the tolerance factor.	12
Table 2. Summary of photovoltaic performance of reference and 2TI/4TmI passivated devices	57

LIST OF FIGURES

Figure 1.1 Fossil fuel consumption per capita, 2022. Fossil fuel consumption per capita is measured as the average consumption of energy from coal, oil and gas per person. Data source: Energy Institute Statistical Review of World Energy (2023).	1
Figure 1.2 Comparison of electricity consumption from fossil fuels, nuclear and renewable sources. Data source: Energy Institute Statistical Review of World Energy (2023).	2
Figure 1.3 Best Cell-Efficiency chart highlighting the growing appeal of Perovskite solar cells. Data Source: NREL chart[4].	5
Figure 1.4 Benefits of perovskites as energy materials Source: ACS Energy Lett. 2022, 7, 8, 2490-2514[3].	6
Figure 1.5 Schematic summarizing the chapters and topics of this dissertation.	9
Figure 2.1 Lead halide perovskite structure ABX_3- A, B, and X site in the perovskite structure.	11
Figure 2.2 Electronic structure of defect intolerant semiconductors versus defect tolerant lead halide perovskites. Source: Chem. Mater. 2017, 29, 4667-4674 [18].	13
Figure 2.3 3D network of corner sharing octahedra in perovskites.	14
Figure 2.4 Lower dimensional Ruddlesden- Popper phase with inorganic lead halide planes separated by the organic molecules.	15
Figure 2.5 Spin coating method used to deposit perovskite active layer and passivation layers in this work. While the perovskite solution spread out on the underlying charge transport layer (such as TiO_2 for ETL) is spin coated, the anti-solvent is dropped dynamically, followed by annealing to achieve the photoactive black perovskite phase.	17
Figure 2.6 Perovskite solar cell in n-i-p architecture.	18
Figure 2.7 Temperature dependent structural transformations in metal halide perovskites. Reprinted with permission from [65] Copyright © 2021, American Chemical Society.	21
Figure 2.8 Common surface defects in lead halide perovskite thin films	24
Figure 2.9 Bulky organic cations such as phenethylammonium iodide (PEAI) form a protective barrier over perovskite surface for moisture resistance.	25
Figure 2.10 Long chain conjugated ammonium ligands used in this work.	28

Figure 3.1 A typical XPS spectra for Pb 4f obtained from CsFAPbI₃ thin film.	31
Figure 3.2 A typical surface SEM image of CsFAPbI₃ film. Scale bar is 1μm.	32
Figure 3.3 A typical GIWAXS 2D pattern (left) and intensity profile (right) for 2TI passivated perovskite film annealed for 10 minutes at 100$^{\circ}$C.	33
Figure 3.4 Mechanism of X-ray excited optical luminescence	34
Figure 3.5 Mechanism of X-ray beam induced current. Instead of recombining, the charge carriers are extracted by charge selective electron and hole transport layers.	35
Figure 3.6 Schematic of electron energy levels near the surface of a clean semiconductor: (a) intrinsic semiconductor; (b) disequilibrium and (c) equilibrium between n-type bulk and its surface; (d) disequilibrium and (e) equilibrium between p-type bulk. Reprinted with permission from [96] Copyright 2012 American Chemical Society.	36
Figure 3.7 Band flattening observed as surface photovoltage measurements using kelvin probe force microscopy technique.	37
Figure 4.1 Film morphology seen in SEM images for 2TI- 0; 2TI-40 and 4TmI-0; 4TmI-40 films. 0 and 40 are annealing times at 100C. Scale bar is 1μm.	41
Figure 4.2 XPS spectra for Pb 4f and N 1s for reference (black) versus passivated films- 2TI (top) and 4TmI (bottom).	43
Figure 4.3 GIWAXS intensity profiles comparing reference perovskite with 2TI (left) and 4TmI (right) passivated films.	44
Figure 5.1 Surface Photovoltage histogram. For contact potential distributions showing potential spread and mean used for SPV (CPD_mean(light)- CPD_mean(dark)), refer to figure A9	50
Figure 5.2 Charge extraction and recombination in Reference, 2TI and 4TmI films after 40 min annealing at 100 $^{\circ}$C.	52
Figure 5.3 Statistics of device performance for perovskite solar cells with different passivation layers (a) device schematic, (b) V_{oc}, (c) J_{sc}, and (d) PCE (mean PCE is shown beside the boxes). Device parameters are obtained from reverse J–V scans.	56
Figure A1. Spin coating method used to deposit perovskite and passivation layers. 4mM solutions of 2TI (1.35mg/mL) and 4TmI (2.12mg/mL) dissolved in isopropyl alcohol were spin coated on CsFAPbI₃ thin films.	63
Figure A2. Surface morphology of the perovskite films treated with Ref, 2TI and 4TmI (top to bottom) after 0, 10 and 40 minutes annealing (left to right). Scale bar is 1μm.	64

Figure A3. XPS elemental scans for Pb 4f, N 1s, I 3d, C 1s and S 2p on the top surface of perovskite films treated with 2TI molecules.....	65
Figure A4. XPS elemental scans for Pb 4f, N 1s, I 3d, C 1s and S 2p on the top surface of perovskite films treated with 4TmI molecules.	66
Figure A5. GIWAXS profiles show changes in crystal structure of the interfaces treated with 2TI and 4TmI (top to bottom) after 0-, 10- and 40-minutes annealing (left to right)..	67
Figure A6. Comparison of surface versus bulk crystallinity of 2D (2T)₂PbI₄ and (4Tm)₂PbI₄ layers after 40 min anneal.	67
Figure A7. Evolution of the 2TI and 4TmI layer in bulk with annealing.....	68
Figure A8. Spatial maps showing Contact Potential Distributions in dark and light.	69
Figure A9. Contact Potential Distributions showing potential spread and mean used for SPV (CPD_mean(light)- CPD_mean(dark)).....	70
Figure A10. Surface Photovoltage histogram.....	70
Figure A11. Topography of reference versus passivated perovskite.	71

LIST OF SYMBOLS AND ABBREVIATIONS

PSC	Perovskite Solar Cell
OECD	Organization For Economic Co-Operation And Development
PV	Photovoltaic
CdTe	Cadmium Telluride
CIGS	Copper Indium Gallium Selenide
DSSC	Dye-Sensitized Solar Cells
OPVs	Organic Photovoltaics
VB	Valence Band
CB	Conduction Band
FA	Formamidinium
MA	Methylammonium
HOMO	Highest Occupied Molecular Orbital
LUMO	The Lowest Unoccupied Molecular Orbital
CBM	Conduction Band Minima
VBM	Valence Band Maximum
RP	Ruddlesden Popper
DJ	Dion-Jacobson
ACI	Alternating Cations In The Interlayer
DMF	Dimethyl Formaldehyde
DMSO	Dimethyl Sulfoxide

ETL	Electron Selective Layer
HTL	Hole Selective Layer
TCO	Transparent Conductive Oxide
FTO	Fluorine-Doped Tin Oxide
Spiro-OMeTAD	2,2',7,7'-Tetrakis[N,N-Di(4-Methoxyphenyl)Amin]-9,9'-Spirobifluoren
Au	Gold
PVA	Polymer Ethylene-Vinyl Acetate
MPP	Maximum Power Point
CTE	Coefficients Of Thermal Expansion
P3HT	Poly(3-Hexylthiophene)
PTAA	Poly[Bis(4-Phenyl)(2,4,6-Trimethylphenyl)
PEAI	Phenethyl Ammonium Iodide
EPN	Ethyl P-Nitrobenzoate
IPA	Isopropyl Alcohol
DI	De-Ionized
TBP	Tert-Butylpyridine
2TI	2-([2,2' bithiophen]-5-yl)ethan-1-ammonium iodide
4TmI	2-(3'',4'-dimethyl-[2,2':5',2'':5'',2'''-quaterthiophen]-5-yl)ethan-1-ammonium iodide
XPS	X-Ray Photoelectron Spectroscopy

SEM	Scanning Electron Microscopy
GIWAXS	Grazing Incidence Wide Angle X-Ray Scattering
XEOL	X-Ray Excited Optical Luminescence
XBIC	X-Ray Beam Induced Current
FWHM	Full-Width-Half-Maximum
KPFM	Kelvin Probe Force Microscopy
AFM	Atomic Force Microscopy
SPV	Surface Photovoltage
FF	Fill Factor
PCE	Power Conversion Efficiency
AM	Air Mass
SI	Supplementary Information
DFT	Density-functional theory
LDP	Lower Dimensional Perovskite
CPD	Contact Potential Difference
DC	Direct Current
PL	Photoluminescence
V_{oc}	Open-Circuit Voltage
J_{sc}	Short-Circuit Current

SUMMARY

Photovoltaic technology has been proposed as a promising alternative to reduce the dependence of our world's growing population on traditional fossil fuels. To accomplish this, lead halide perovskite solar cells (PSC) have emerged as promising next generation photovoltaic devices. They have ideal optoelectronic properties and have shown significant improvements in power conversion efficiencies exceeding 25%. Despite their growing appeal, device instability is a major commercialization bottleneck that has prevented their widespread use. Perovskite solar cells have a sandwich architecture with several interfaces between the active perovskite layer and adjacent charge transport layers. These interfaces are prone to defects which accelerate the degradation of perovskite materials under environmental stressors such as heat, moisture, or oxygen, limiting their long-term viability. Interfaces are also vulnerable to energy level mismatches and play a vital role in influencing charge generation, transport, collection, and recombination mechanisms in devices.

Research on stability enhancement in perovskite solar cells has focused on interface modification to passivate surface defects, protect the bulk of perovskite from external environment by acting as a barrier and tuning the charge transfer properties at the surface. Among the plethora of passivation agents reported in literature, using conjugated organic ammonium molecules have exhibited benefits of hydrophobicity on the sensitive perovskite film and efficient charge delocalization brought on by the conjugated structure. However, most interface modification strategies relying on organic molecules introduce an electrically insulating spacer layer under thermal stress. Heat induced diffusion of molecules can reconstruct the interface into lower dimensional phases, which impedes charge extraction and affects photo-conversion efficiency (PCE) of devices. This brings a tradeoff between the benefits of passivation and charge extraction.

For proper interface design, it is essential to study the thermal behavior of these passivation layers and establish their relationship with the optoelectronic properties of solar cells. The purpose of this thesis is to explore the role of bulky passivation agents on interface stability and charge extraction using long chain thiophene functionalized π -conjugated molecules such as 2TI and 4TmI, which possess two and four thiophene rings, respectively. This work explores the nature of passivated perovskite/hole transport layer interfaces under thermal stress and finds that decreasing the length of the cation backbone accelerates the rate of reconstruction of interfacial perovskite structure, evident in faster phase conversion in 2TI passivation layer versus the larger sized 4TmI. The role that oligothiophene tail plays in determining the spacer layer conductivity and prompting different localized charge extraction and recombination behaviors in 2TI versus 4TmI passivated devices has been highlighted. Results will show that despite the observed phase changes, 2TI treated devices can tune the surface potential to promote efficient holes extraction and reduce recombination. In conclusion, these superior properties brought on by interfacial steric engineering will result in increased 2TI/CsFA based solar cell efficiency of 20.13%.

By identifying the nature and impact of heat induced dynamical structural changes at passivated perovskite interfaces, this work highlights the key to surface functionalization so that solar cell performances can be maintained at high operating temperatures.

CHAPTER 1. INTRODUCTION

1.1 Growing Energy Demand

Climate change is one of the most daunting socio-economic challenges of the 21st century. It has affected wildlife, biodiversity, and human communities, with people in developing countries most at risk of facing its adverse effects on health, access to clean water, agriculture, and overall quality of life. Burning of fossil fuels- coal, oil, gas- to generate power leads to emission of greenhouse gases which is by far one of the main factors behind climate change. Figure 1.1 highlights the severe consumption of fossil fuels in kilowatt-hour by countries across the globe.

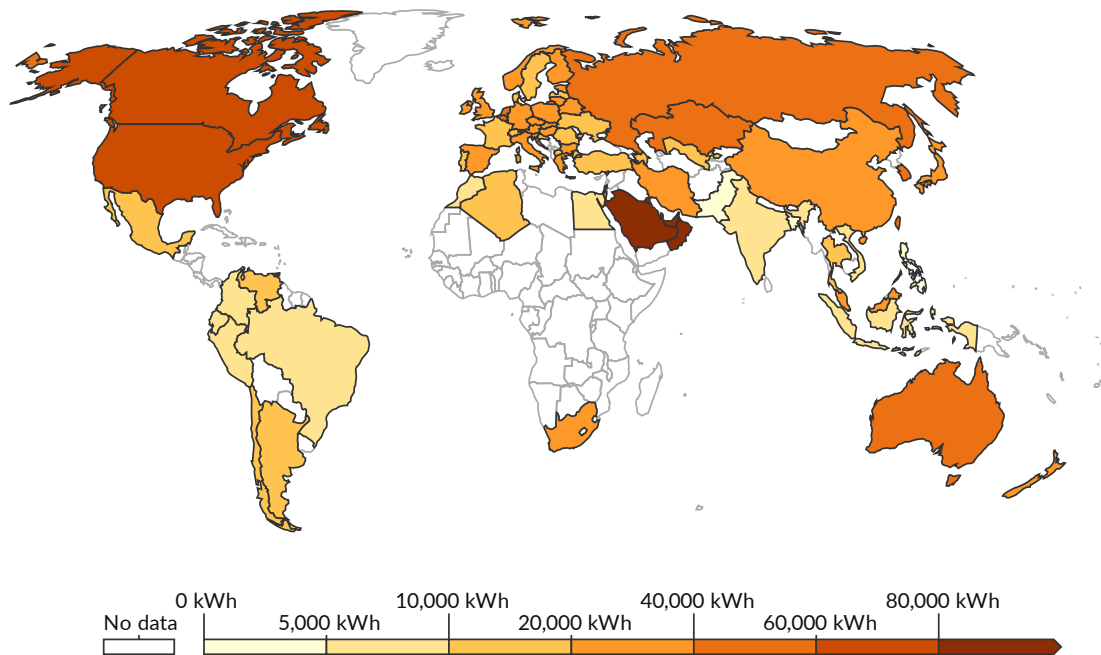


Figure 1.1 Fossil fuel consumption per capita, 2022. Fossil fuel consumption per capita is measured as the average consumption of energy from coal, oil and gas per person. Data source: Energy Institute Statistical Review of World Energy (2023).

Thanks to the measures and incentives implemented to promote the integration of renewable energy sources, the share of renewable energy production within the Organization for Economic Co-operation and Development (OECD) countries has risen from 21.7% in 2012 to 31.2% in 2022[1]. Despite this positive trajectory, fossil fuels still dominate global energy production in comparison to renewable energy sources for most developed countries (Figure 1.2), posing a substantial obstacle to achieving a comprehensive shift towards clean energy.

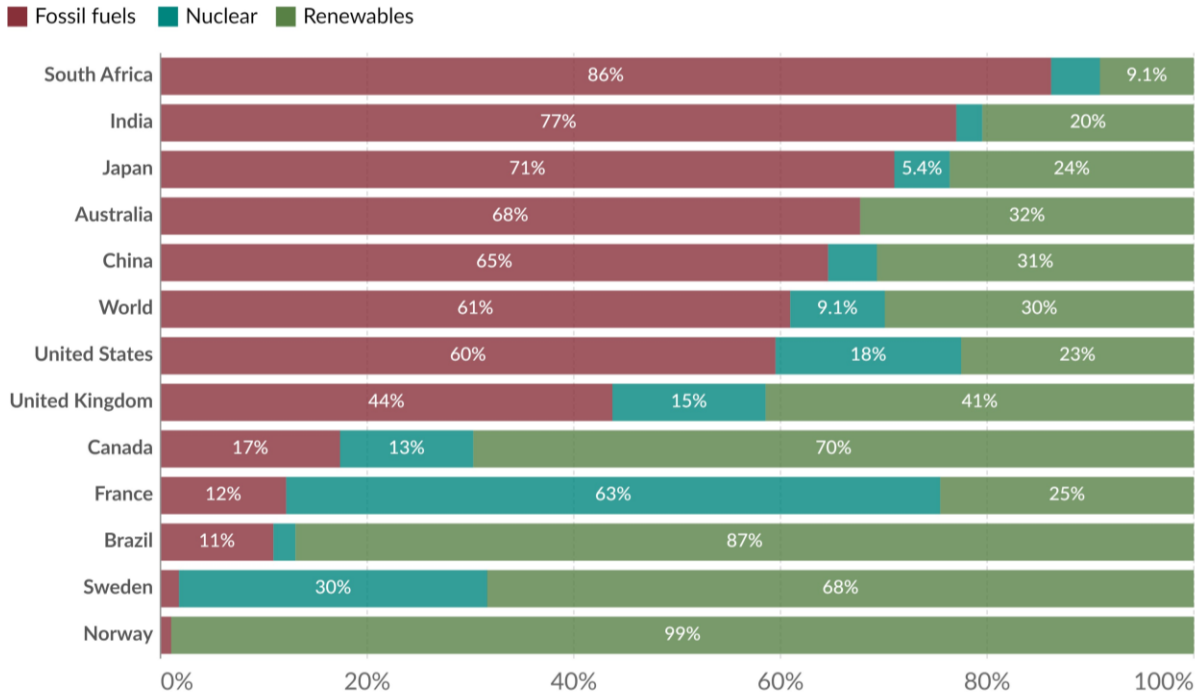


Figure 1.2 Comparison of electricity consumption from fossil fuels, nuclear and renewable sources. Data source: Energy Institute Statistical Review of World Energy (2023).

Given the urgent need for renewable energy sources, solar photovoltaics- which capture energy from the sun and convert it to electricity, stand out as a promising solution. Solar energy has, in principle, zero carbon dioxide emissions, infinite resource availability in the form of sun’s

energy, and versatile applications in both industrial and residential settings. Of special importance to developing countries is the fact that solar panels can be installed on small rooftops, allowing remote areas to access electricity without having to rely on centralized power grids.

As the second most abundant material on Earth, Silicon is by far the most used semiconducting material for global PV production, dominating the market with about 95% share in solar modules production[2]. It is also the most used component in microelectronics due to its high energy efficiency and long lifespan. However, present use of silicon for PV applications presents certain long-term challenges such as resource deficiency, the difficulty and cost associated with mining the element as well as removing impurities in recycled Si panels[3]. In addition, while the current industrial infrastructure is set up to support Si based PV modules, they have a high manufacturing cost due to the need for extremely high purity Si wafers and high temperature processing. Silicon solar panels are also rigid, limiting their use in applications requiring flexible substrates, such as portable devices.

In response to these limitations, perovskite solar cells have emerged as strong candidates to replace or be used in tandem with pure Silicon based solar cells. Promising trends have been observed in perovskite solar cell performances with efficiencies exceeding 25% for perovskite with ongoing promising research in device optimization[4]. PSC/Si tandem devices benefit from advantages offered by both materials- utilizing the existing pilot line set ups for Si modules and the ideal PV characteristics of perovskites. As of 2022, perovskite silicon tandem cells have exceeded 30% efficiency for small area devices[5].

1.2 Evolution of Photovoltaic technology

In response to the evolving needs for higher efficiency and performance, solar cells have evolved from p-n junction silicon solar cells to those using perovskites as the active layer.

First generation solar cells made of silicon played a foundation role in the evolution of solar technology. These solar cells use mono- or poly- crystalline silicon to absorb photons and generate electron-hole pairs. They offer high module efficiencies (>20%) and retain more than 80% of their initial power after an operational lifetime of 25 years. They also have an ideal bandgap of 1.12eV for outdoor PV applications and have dominated the PV market for over 30 years[6]. However, they face several limitations. First, growing large single crystals of silicon is an extremely controlled and energy intensive process which significantly adds to the production cost. Second, their low absorption coefficient necessitates thick active layers to ensure that adequate sunlight is absorbed for satisfactory performance, making the overall module bulky. This limits their versatility in applications in lightweight structures where weight is a concern. Third, electronic grade silicon must of extremely high purity to provide high efficiencies, necessitating multiple costly metallurgical refining steps to recover silicon at the end of a solar panel's lifetime[7]. These notable limitations have propelled the emergence of next generation solar cells.

Second generation solar cells consist of Cadmium Telluride (CdTe), Copper Indium Gallium Selenide (CIGS) and amorphous silicon. They can be made of very thin films on a variety of substrates including glass or plastics, which offer enhanced flexibility and lightweight, widening their applications in building integrable photovoltaics[8]. They also have less energy intensive and more cost-effective manufacturing, resulting in more affordable solar panels. However, challenges include first, environmental concerns associated with proper handling and disposal of cadmium- a toxic heavy metal, rarity of metals such as tellurium which is 300,000,000 times less abundant

than silicon for CdTe solar cells and indium for CIGS solar cells[9]. a-Si solar cells also suffer from low efficiencies with record 14% [10].

Third generation solar cells include dye-sensitized solar cells (DSSC), organic photovoltaics (OPVs) and perovskite solar cells (PSCs). They face commercialization challenges related to heat and light induced instabilities and structural degradation. Despite this, PSC in particular have shown increasingly high efficiencies, exceeding 25% by the end of the last decade per the NREL efficiency chart (Figure 1.3) [4]. They offer advantages of tunable bandgap, which makes them useful for a range of applications beyond solar cells such as biosensors and photodetectors, in addition to easy fabrication is scalable to industry for large scale production. This chapter highlights the unique structure and optoelectronic properties of PSCs as well as key stability challenges that limit their use in ambient environments.

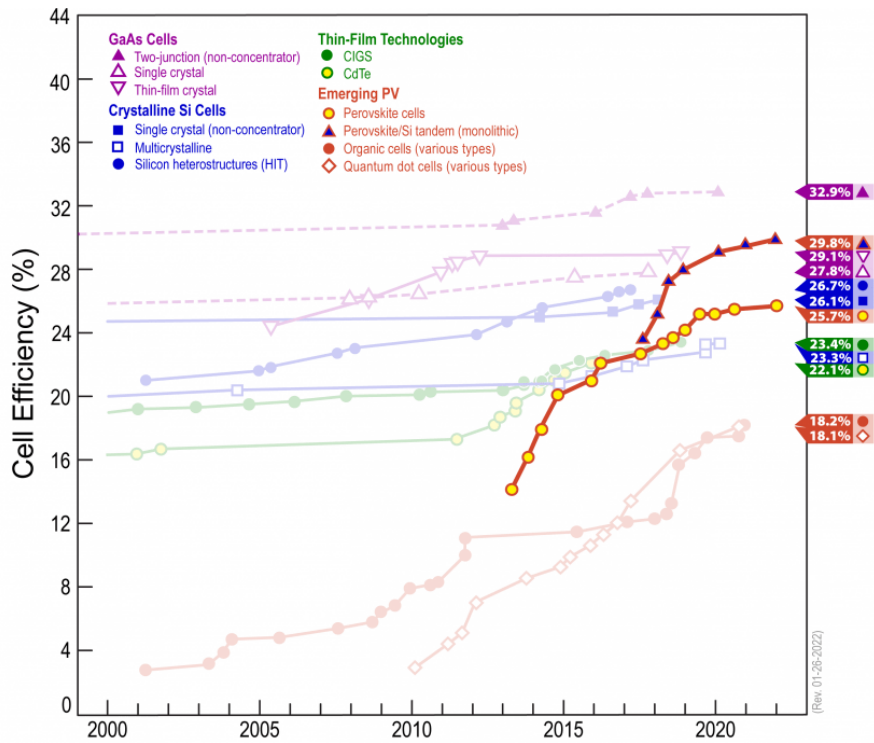


Figure 1.3 Best Cell-Efficiency chart highlighting the growing appeal of Perovskite solar cells. Data Source: NREL chart[4].

1.3 Perovskite Solar Cells- An overview

Metal halide perovskite semiconductors have grown in popularity as the active materials in solar cells due to their remarkable properties. The organic-inorganic hybrid perovskite materials open the possibility of composition tuning, which in turn helps tune their energy bandgap[11]. This means that these materials can be used to absorb the desired wavelengths on the energy spectrum. Perovskites can be fabricated using a simple spin coating method from relatively inexpensive raw materials and can be deposited on flexible substrates such as plastics, making them ideal for lightweight electronics integrable into a range of surfaces, from vehicles to buildings[12]. Paramount to the success of perovskite materials is their “defect tolerance”[13]. Perovskites have an unusual band structure where both the valence band (VB) and conduction band (CB) are formed of antibonding orbitals. Due to this, perovskites have been reported to be prone to forming shallow defect states within the CB/ VB or near the band edges as opposed to deeper in the bandgap. This translates to their ability to produce solar cell performance like single crystal silicon despite having an exponentially greater defect density. All these benefits in conjunction make perovskites attractive light absorber materials in solar cells.

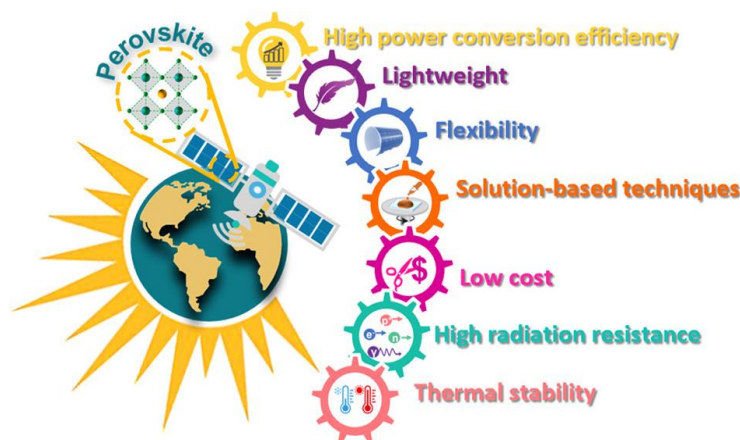


Figure 1.4 Benefits of perovskites as energy materials Source: ACS Energy Lett. 2022, 7, 8, 2490-2514[3]

Lately, much work has been dedicated to stability enhancement in perovskite solar cells. This key area of research poses as a commercialization bottleneck in the goal to achieve 25 years of operational solar panel lifetime. The perovskite solar cell is a stack of different kinds of materials including hole and electron charge transport layers and electrodes. This sandwich structure gives rise to multiple interfaces between the active perovskite layer and the adjacent charge transport layers which are susceptible to degradation for several reasons[14]. The abrupt termination of lattice at the surface gives rise to dangling bonds or lattice imperfections which can serve as trap states to capture photogenerated carriers and induce voltage losses. Charge transfer and extraction can further be affected by energy misalignment between different materials at the interface. Interfaces also act as a pathway for moisture ingress leading to decomposition in the active perovskite layer. To optimize the interfaces and address these challenges, researchers have undertaken interface engineering, incorporating a variety of materials including polymers, organic molecules, and low dimensional materials[15, 16].

Interface engineering enhances stability of perovskite materials on several fronts[14]. It can help inhibit moisture induced degradation by serving as a hydrophobic shield on the perovskite surface. Using a passivation layer can help eliminate surface trap states which contribute to chemical decomposition of perovskite film under oxygen and light exposure. Eliminating surface defects can also suppress ion migration and help reduce charge recombination at the interfaces, thus maintaining open-circuit voltage and efficiency in devices. It has also been demonstrated that under heat, lattice decomposition of perovskite starts at the surface, and functionalizing the surface or using a buffer layer can enhance perovskite film thermal stability[17].

Successful operation of perovskite solar cells under external conditions hinges upon efficient performances of all components of the device. For passivation layers, problems can arise when the films are thermally stressed[18]. The underlying reasons behind their degradation stems from disruption of the 3D perovskite structure and formation of lower dimensional phases due to molecular diffusion[19]. Despite some reports, there is overall a lack of comprehensive understanding into the underlying mechanisms and effects of interfacial structure transformation so induced, as well as the factors that can help control these changes.

1.4 Aim of this thesis

This work will outline an up-and coming approach to interfacial engineering using long chain organic ligands that contribute to improved photo-conversion efficiencies and open circuit voltages in PSCs. This thesis explores spacer cations such as thiophenes that offer conjugated functionality along with the ability to form hydrogen bonds with the inorganic layer so as to enhance the probability of charge transfer[20]. Long chain organic ammonium cations- *2-(2,2'-bithiophen-5-yl)ethan-1-ammonium iodide*, (denoted as 2TI) and *2-(3',4'-dimethyl-[2,2':5',2'':5'',2'''-quaterthiophen]-5-yl)ethan-1-ammonium iodide* (denoted as 4TmI) are used. By using molecules of different sizes, the impact of steric size of long chain thiophene cations on thermal stability at perovskite interfaces is investigated. Tailoring the steric hindrance of the bulky cations used to treat perovskite surfaces presents an opportunity to control cation mobility, and consequently any phase changes resulting at elevated temperatures.

Chapter 4 reviews the first step of the research, which consists of passivating perovskite films with molecules of different sizes (molecular mass) and structures and annealing them to investigate how the perovskite structure evolves over time in response to heating. It demonstrates that despite undergoing structural transformations, devices with passivating molecules consistently

exhibited higher efficiencies compared to their un-passivated counterparts, achieving efficiency exceeding 20%.

Chapter 5 reviews the second step of the research, elucidating the observed performance variations by establishing a correlation between the thermal stability of perovskite films and the size of passivating molecules. This is aimed at finding the balance between minimizing structural instability and maximizing the benefits of defect elimination seen in improved performances. Overall, understanding the structure-property relationships existing between passivation molecules and perovskite active layer will lay the groundwork to resolve the stability challenges in perovskite solar cells.

Chapter 6 concludes this thesis. It summarizes the goals of this work, highlights the important findings, and presents further approaches that can be employed to achieve stable, high-performing PSCs.

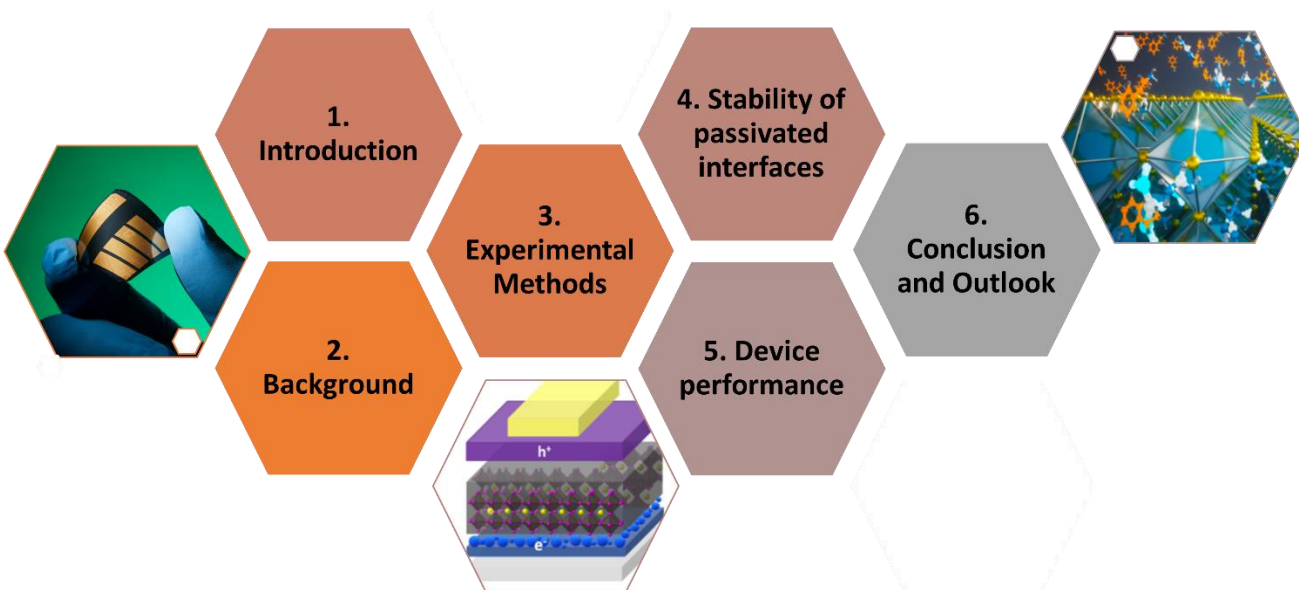


Figure 1.5 Schematic summarizing the chapters and topics of this dissertation.

CHAPTER 2. BACKGROUND

2.1 Properties of Lead Halide Perovskites

Following the discovery of the mineral CaTiO_3 in 1839 by the Russian mineralogist Perovski, perovskites have emerged as a class of semiconducting materials with multifaceted applications [21, 22]. All materials that exhibit the same crystal structure as Calcium Titanate are said to belong to the class of materials called perovskites. They have the general formula ABX_3 where A is a monovalent cation MA, $\text{NH}_2\text{CHNH}_2^+$ (formamidinium, FA), B is a divalent metal cation such as Pb^{2+} and X is a halogen atom. Halide perovskites were reportedly first observed as CsPbX_3 in the 1890s[23]. Owing to their low excitonic properties, high light absorption, solution processability and vast potential for composition and bandgap engineering, they are now widely investigated in the field of optoelectronics for applications such as light emitting diodes[24], solar cells[25], photodetectors[26], and lasers[27]. Different dimensionalities of perovskites have been explored from 3D to lower dimensional materials such as PQDs (0D), nanorods (1D) and nanowires (2D). This work will focus on 3D lead halide perovskites and their derivatives which are the most used materials for PSC fabrication.

2.1.1 Crystal Structure and Optoelectronic Properties

Metal halide perovskites consist of a network of corner sharing $[\text{BX}_6]^{4-}$ octahedra units, wherein the organic FA/MA cation is present in each cuboctahedral void (middle of eight octahedra), as shown in Figure 2.1. Since the $[\text{BX}_6]^{4-}$ units connect through corner sharing, they form a “3D” arrangement. The stability of the perovskite structure depends on the radius ratio of the cations A and B and halogen X , signified by the Goldschmidt tolerance factor ‘ t ’ –

$$t = \frac{r_A + r_X}{\sqrt{2}(r_B + r_X)}$$

$t=1$ is ideal for photoactive cubic phase, also called the black phase. Any deviation from $t=1$ results in formation of non-photoactive delta phase in which the characteristic corner sharing octahedra are absent.

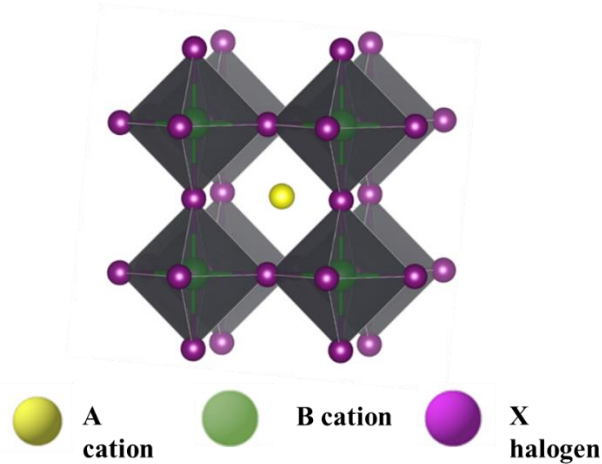


Figure 2.1 Lead halide perovskite structure ABX₃- A, B, and X site in the perovskite structure.

Hybrid organic-inorganic perovskite consisting of mixed composition at A sites such as Cs_xFA_{1-x}PbI₃ provide an exciting opportunity to explore the phase space with varying compositions. Doing so allows tuning the bandgap of the perovskite as well as dimensional tuning to achieve lower dimensional perovskites (2D/1D). It also allows for achieving tolerance factors of 1 that would be otherwise unattainable in pure MAPbI₃ or CsPbI₃ due to ionic radius constraint. Alloying leads to stabilization of cubic phase that is absent in pure FAPbI₃ films at room temperature. The following table summarizes some perovskite lattice structures based on the t factor[11].

Table 1. Examples of perovskite structures based on the tolerance factor.

Lattice Structure	Radii	t-factor
Cubic (SrTiO ₃)	R _A and R _B can be unequal	0.9-1
Trigonal (FeTiO ₃)	R _A =R _B =R _X	<0.7
Hexagonal (BaNiO ₃)	R _A >>R _B	>1
Rhombohedral (CaTiO ₃)	R _A <<R _B	0.75-0.9
Orthorhombic (CaTiO ₃)	R _A <<R _B	0.75-0.9

Compositional tuning of perovskites opens avenues to achieve a wide range of optoelectronic properties. Generally, X and B site doping influences the bandgap and photoluminescence[28], while A- site substitution helps achieve cubic phase stabilization at room temperature. Halide perovskites are direct bandgap semiconductors with high absorption coefficient. Their highest occupied molecular orbital (HOMO) comprises of Pb6s and I5p σ -antibonding orbitals and the lowest unoccupied molecular orbital (LUMO) comprises of Pb6p-I5p π -antibonding and Pb 6p-I 5s σ -antibonding orbitals. B and X orbitals form the conduction band minima while the A cation orbitals do not contribute directly but can influence the structure of the metal-halide framework. Bandgap tuning is a broad area of study and can be accomplished by composition engineering, i.e., X and B site doping [29, 30]. This wide-range bandgap tuning allows perovskite application as photodetectors and in different solar cell architectures.

Another factor that makes perovskites such as MAPbI₃ and related compounds ideal photovoltaic materials is their “defect tolerance”[31]. In conventional semiconductors, the valence band maximum (VBM) is formed by bonding orbitals, and the conduction band minimum (CBM) is formed by antibonding orbitals[32]. When these bonds break, defects in the form of dangling

bonds form near the original bond locations, creating deep defects within the semiconductor bandgap (Figure 2.2, left). Perovskites, on the other hand, derive their bandgap from antibonding orbitals at both the VBM and CBM. Consequently, breaking these bonds results in the creation of either shallow defects or trap states within the valence band. These shallow states do not significantly lead to non-radiative recombination, which makes perovskites resilient to very high defect densities[22]. However, the drawback is that elevated defect densities lower the energy barrier for ion migration through the film which accelerates the degradation of the absorber.

Further work is being done on exploring this characteristic to give a more complete understanding of the underlying reasons[13, 33]. Their defect tolerance also contributes to long carrier diffusion lifetimes in perovskites, leading to high current generation by allowing time to the photoexcited carriers to diffuse to charge transport layers before recombination mechanisms become active.

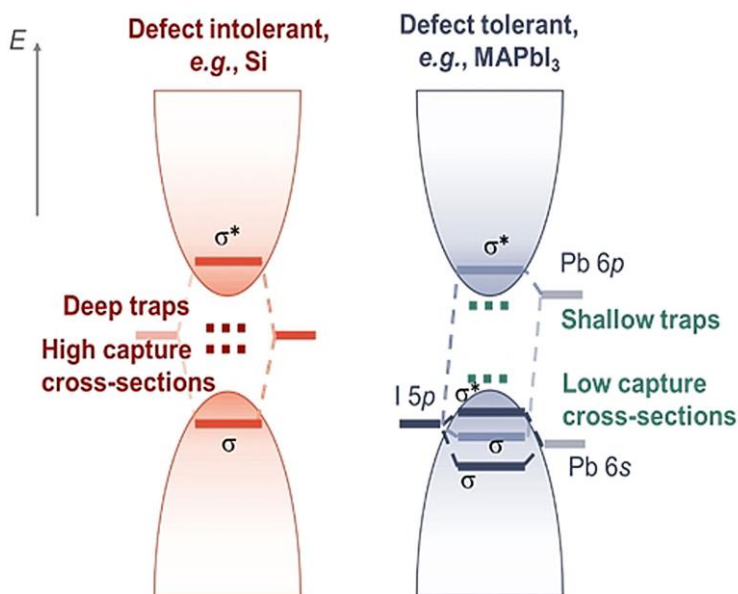


Figure 2.2 Electronic structure of defect intolerant semiconductors versus defect tolerant lead halide perovskites. Source: Chem. Mater. 2017, 29, 4667-4674 [18]

2.1.2 Perovskite Dimensionality

“3D” perovskites are bulk materials that have a corner sharing arrangement of $[BX_6]^{4-}$ octahedral units extending in all dimensions, as shown in Figure 2.3. This spatial arrangement in 3D perovskites can be modified to give rise to “low dimensional” perovskite phases which refers to structures with at least one dimension confined to the molecular level. Based on the separation between these layers and the number of layers (referred to as n), materials possess different electronic and charge transfer properties, and have also been explored for solar cells in literature[34].

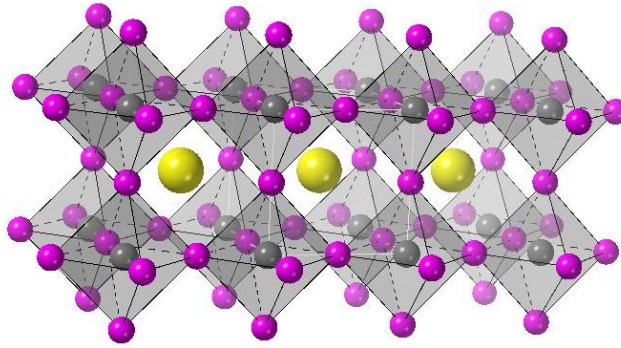


Figure 2.3 3D network of corner sharing octahedra in perovskites.

2D or quasi 2D structures are obtained by incorporating bulky organic cations as spacer molecules to separate metal halide BX_6 layers which are held together by Van der Waals forces[35]. These structures are termed Ruddlesden Popper (RP) phases. They have the general chemical formula $A_{n-1}A'_2B_nX_{3n+1}$ where A is the small cations in the voids within a metal halide layer, A' is a large organic cation between adjacent layers and n refers to the number of metal halide monolayers. $n = \infty$ refers to 3D perovskites. Commonly used cations in RP phase consist of alkyl chains or phenyl groups with monovalent ammonium functional group[36]. The

inorganic BX_6 layers in RP perovskites are separated by two layers of these cations and show an offset in stacking in both a and b directions.

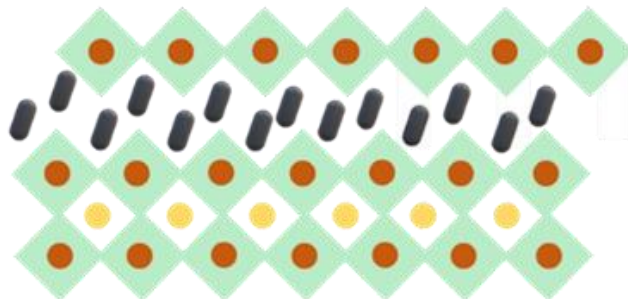


Figure 2.4 Lower dimensional Ruddlesden- Popper phase with inorganic lead halide planes separated by the organic molecules.

Based on the functionalization of the organic cation, 2D structures of Dion-Jacobson (DJ) type or alternating cations in the interlayer space (ACI) type have also been explored[37, 38]. Low dimensional layered perovskites show the formation of quantum well structures with the inorganic BX_6 layers acting as potential wells confined by photo-inactive organic spacer or “barrier”. The length of quantum well (the n value) and the barrier layer determine the extent of quantum confinement in these structures; wherein charge transport through the organic spacer is severely restricted in the out of plane direction. Despite showing greater structural stability than their 3D counterparts, 2D perovskites have shown limited PCEs in devices owing to poor charge transport and large bandgap[39, 40]. However, by controlling the number of inorganic layers and the interlayer spacing, bandgap of lower dimensional R-P perovskites can be tuned. These factors in turn can be modified by varying the length of organic molecule used to template the 3D structure[41]. As such, to resolve performance issues in 2D perovskites and the instabilities in 3D

perovskites, hybrid 3D-2D perovskite structure has been utilized, which afford improved moisture stability in addition to enhancements in device properties[42, 43].

2.1.3 Perovskite Solar Cell Fabrication

The most popular method of perovskite thin film fabrication for research in laboratories is spin coating, due to its ease of operation and optimization in addition to cost- effectiveness. However, this method is not appropriate for large scale fabrication and multiple other methods based on both solution processing and vacuum evaporation have emerged.

Spin-coating method coats a substrate with liquid perovskite solution by the centrifugal force of the rotating substrate. This method results in films with high quality and uniform morphology using anti-solvent technique. The perovskite solution is prepared by mixing stoichiometric ratio of organic halide and lead halide salts into a solvent such as DMF/DMSO, mixed in an optimized ratio. If Cs doping is required, Cesium Iodide is also mixed in the solution. During spin coating, the anti-solvent (commonly toluene or chlorobenzene) is dripped onto the substrate at a fixed time. The exact time of introducing the anti-solvent is important as it contributes to crystallization kinetics, grain size and defect density in the perovskite film being deposited. Commonly, the films are thermally annealed after spin coating to evaporate the residual solvent convert intermediate yellow (orthorhombic) phase to black (cubic) photoactive phase [44].

If necessary, post treatment can be done by depositing passivation layers over the perovskite. A typical process using an anti-solvent is schematically shown below.

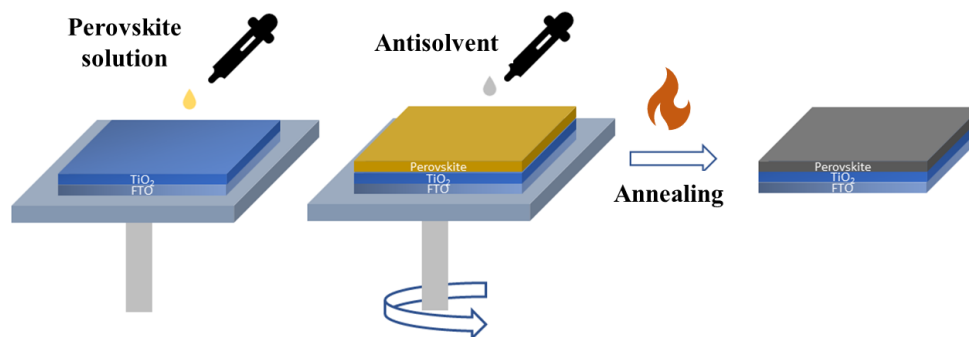


Figure 2.5 Spin coating method used to deposit perovskite active layer and passivation layers in this work. While the perovskite solution spread out on the underlying charge transport layer (such as TiO₂ for ETL) is spin coated, the anti-solvent is dropped dynamically, followed by annealing to achieve the photoactive black perovskite phase.

The solar cell operates on the principle of the photovoltaic effect, generating a voltage across a material when exposed to light. First, the light-harvesting material- perovskite in this case- absorbs photons and generates electron-hole pairs. Subsequently, these electrons and holes are separated within the device, enabling electron flow through an external circuit. In the context of Perovskite Solar Cells (PSCs), the perovskite absorber layer is situated between electron and hole selective layers (ETL and HTL, respectively). The device incorporates two electrodes on each side of the selective contacts to complete the electric circuit. The architectural configuration of PSCs can vary based on the chosen HTL and ETL. In the solar cells examined within this dissertation, an n-i-p architecture is employed, with the ETL facing the illumination source at the bottom (refer to Figure 2.6). The bottom electrode is composed of a transparent conductive oxide (TCO), specifically fluorine-doped tin oxide (FTO). Serving as the ETL, a thin and compact titanium

dioxide layer (c-TiO₂) is utilized in conjunction with a top mesoporous anatase (mp-TiO₂) polymorph. The HTL, responsible for facilitating hole transport, is the molecule 2,2',7,7'-Tetrakis[N,N-di(4-methoxyphenyl)amin]-9,9'-spirobifluorene (Spiro-OMeTAD). The top electrode is made of gold (Au). PSCs manifest as a layered structure, underscoring the importance of studying interfaces and selective contacts within these devices for a comprehensive understanding and optimization of this technology.

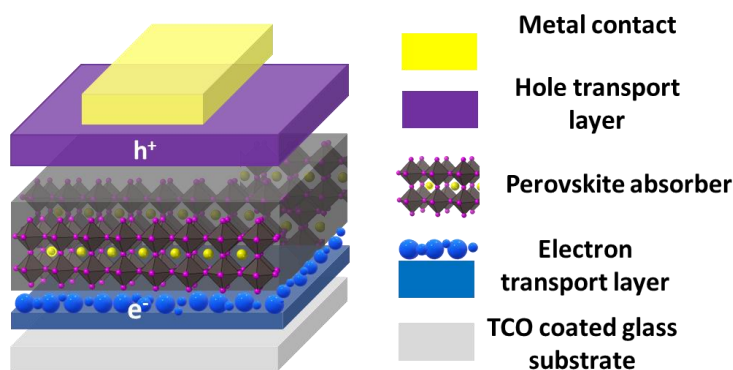


Figure 2.6 Perovskite solar cell in n-i-p architecture.

For large area perovskite film fabrication, methods such as doctor blade or spray coating, or vacuum based thermal evaporation have been used[45]. Doctor blading method involves dropping the precursor solution at one end of the substrate and using a blade to linearly raster over the entire substrate, dragging the solution to uniformly coat the substrate. This method has the potential to produce over foot-scale dimensions with controlled thickness and minimal material waste[46]. Several works have attempted to improve the quality of doctor bladed films. It has been shown by Mallajosyula et al. that the crystalline quality and phase of the perovskite film deposited using this method can be controlled by optimizing the substrate-blade distance, precursor solution viscosity, blade speed as well as the temperature of the substrate[45].

Spray coating consists of fluidic ink being ejected as drops from a spray gun and deposited on the substrate by force of gravity. This method is low cost, can be applied to substrates regardless of their size and is suitable for scalable manufacturing of conformal, homogeneous large area thin films[47, 48]. To ensure that issues related to incomplete coverage do not arise, the spray jet pressure needs to be unvarying. The atomization of fluid into droplets in a desired direction on large area substrates can be done by utilizing a high flow carrier gas such as Oxygen that helps carry the subject fluid. The high momentum allows droplets to be deposited while the carrier gas flows around. Spray coating is a versatile method that can also be used to deposit electron transporting layers (ETL), hole transport layers (HTL) and electrodes[49-51], in addition to the perovskite active layer.

Thermal Evaporation is a vapor deposition method that takes place under a high vacuum. A solid material is electrically heated to above its sublimation temperature such that the vapors travel in vacuum and condense onto the substrate. The deposition rate, which influences the perovskite crystal growth, is sensitive to chamber pressure, distance between the source(s) and the substrate[52]. Deposition can either be one step- where all individual precursors or the desired product prepared beforehand are evaporated at once; or multi-step, where deposition proceeds in several steps, each precursor being evaporated in turn[53]. This has led to several variants of this methodology including co-evaporation, flash evaporation and sequential evaporation. This process enables careful control of deposition rate to obtain smoother films with fine grains. Perovskite films deposited by thermal evaporation do not require additional annealing step to convert to cubic phase. At the same time, this method necessitates optimizing the source evaporation recipes which are different for each precursor and time consuming. It can also lead to contamination issues on repeated operation due to precursor deposition on chamber walls during evaporation[54].

2.2 Perovskite degradation mechanisms and stability approaches

Perovskite solar cells face an enormous challenge when it comes to commercial deployment due primarily to their instability in ambient conditions. When exposed to hot and humid environments, perovskites interact with atmospheric oxygen and moisture, leading to structural degradation[17]. Encapsulation has been employed as a solution to isolate the perovskite from environmental stressors by forming a physical barrier. Capping layers formed from MgF_2 , polyolefin, polymer ethylene-vinyl acetate (PVA), butyl rubber edge seal have been reported to act as good encapsulants to withstand heat and moisture[55, 56]. However degradation of perovskite and effects on PSC performance have been reported even after encapsulation[57], demonstrating the need to stabilize perovskites intrinsically. The following paragraphs highlight some mechanisms responsible for instabilities in perovskite solar cells under high temperature and moisture and introduce the surface engineering strategy explored in literature to tackle these challenges.

2.2.1 Stability under heat

Temperature is a crucial factor in PSC manufacturing and operation. Previous reports have shown the influence of operational temperature on the stability of devices, highlighting that even if no significant initial degradation is seen at 20°C over 200 hours of maximum power point (MPP) tracking, increasing the temperature to 50°C or 65°C results in rapid degradation within 100 hours of exposure[58, 59]. Several reasons can be responsible for degradation of perovskite performance under heat.

First, in the range of temperatures required for PSC applications (-15°C to 65°C), several perovskite phases can exist (orthorhombic, tetragonal, cubic). Phase segregation is a major cause of instability in photoactive perovskite phases, limiting its use in ambient atmosphere. Several

strategies have been explored to improve phase stability. Deretzis et al investigated the physical characteristics that determine the phase equilibrium between the yellow and black perovskite phase in CsFAPbI₃ and found that electron doping and spatial confinement at nanoscale play a major role in phase stabilization at room temperature[60]. Their experimental and theoretical studies conclude that these phase stabilizing characteristics can be achieved by optimizing the stoichiometry of precursor solutions, using for example, mixed halide precursor solutions. Composition engineering, i.e. utilizing mixed cation or halogen sites to tune the t-factor has shown to be effective in stabilizing desired phases[61, 62]. For example, pure FAPbI₃ is structurally unstable at room temperature and exists in photo-inactive non-perovskite yellow or delta phase. To stabilize the photoactive “black” phase in FAPbI₃, a small amount of Cesium (Cs) can be incorporated in the precursor solution[63]. Based on this strategy, Saliba et al have reported a high 21% PCE for mixed triple cation PSC[64]. Room temperature favors the formation of orthorhombic phase, followed by tetragonal and cubic phase as temperature is increased. These structural changes triggered in perovskites with temperature are shown in Figure 2.7.

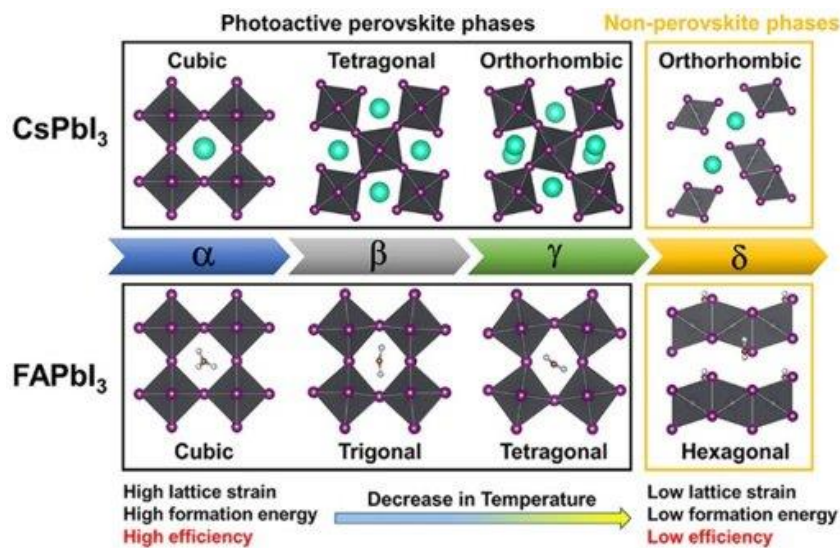


Figure 2.7 Temperature dependent structural transformations in metal halide perovskites. Reprinted with permission from [65] Copyright © 2021, American Chemical Society.

Second, differences exist in the coefficients of thermal expansion (CTE) between the perovskite and the glass substrate. Following spin coating, the perovskite film is annealed to convert to photoactive phase and then cooled down to room temperature. During this thermal cycling, the substrate, with a lower CTE, constrains the perovskite film from contracting. This generates lattice strain in the film, which can lead to fracture in devices during further processing/operation[66, 67]. Under continual thermal stress, strain accumulation due to mismatch in CTE can also lead to delamination of layered PSC structure[68].

Finally, ion migration under heat is another widely reported phenomenon that contributes to lowered stability and hysteresis under long term operation[69]. In lead halide perovskites such as MAPbI₃ and FAPbI₃, I⁻ is reported to be the most likely ionic species to migrate due to short jumping distances to the neighboring vacant sites and low active energy for formation of iodine vacancies[70]. At elevated temperatures, the rate of migration of ions originating from the active perovskite layer increases rapidly, meaning that ions can penetrate the perovskite/CTL and CTL/electrode interfaces. This degrades the quality of the interface due to generation of surface atomic defects. In addition, the migrated halide ions can chemically react with the top electrode, generating reaction products such as lead iodide (PbI₂)[71]. Thermal stress has also been shown to induce changes in charge transport layers- commonly used HTL polymer 2,2',7,7'-Tetrakis[N, N-di(4-methoxyphenyl)amino]-9,9'-spirobifluorene (Spiro-OMeTAD) tends to outgas or crystallize under heat, forming voids to allow a path for gaseous iodine to escape from the underlying perovskite layer[72]. MA⁺ can also penetrate Spiro, introducing deep trap states and deteriorating its hole transport ability[73]. In response to this, alternative organic HTM such as poly(3-

hexylthiophene) (P3HT) and poly[bis(4-phenyl)(2,4,6-trimethylphenyl) (PTAA) are proposed to mitigate the instability resulting from presently used materials[74, 75].

2.2.2 Stability in air

Air induced degradation of perovskite materials is brought about by invasion of foreign species such as oxygen and moisture from air, which causes reactions with the host species. In presence of water, the volatile A site Methylammonium cations (MA^+) react with water, weakening the $\text{PbX}_6\text{-MA}$ bond. HI gas can also be produced resulting from the protonation of I⁻ in the octahedra in air[17]. An alternative to volatile MA is the use of FA or Cs cations but requires composition engineering as discussed previously for phase stabilization. A promising strategy to mitigate air instability in perovskites includes surface treatment of the perovskite film by depositing a passivating layer of bulky organic molecules. Liu et al explored the benefits of a two-dimensional phenethyl ammonium iodide (PEAI) layer to modify perovskite surface[76]. Due to its hydrophobicity, PEAi forms a shielding layer that protects the perovskite film from moisture ingress and helps preserve the original PCE of devices after 65 days in a 15% relative humidity environment. Car et al. used thiol containing ligands at perovskite/HTL interface to block the pathways of moisture diffusion, and found that, compared to the reference device, ligand modification delayed the color change (from black to yellow) of perovskite film when stored in air at room temperature with 45% humidity for 8 days[77].

2.2.3 Interfacial Engineering in Perovskite solar cells

Perovskite solar cells have a layered structure with interfaces between the charge transport layers (CTL) and the active perovskite layer. It is important to optimize the interfaces due to several reasons. First, interfaces are prone to atomic defects due to abrupt termination of lattice periodicity in the bulk of a material. Due to the ionic nature of lead halide perovskites, halide

defects such as iodine vacancies with low energies of formation are easily formed on the surface of the films, in addition to other defects as shown in Figure 2.8. These defects constitute trap states in the bandgap and can become centers for non-radiative recombination. Sherkar et al. reported in their simulations that mitigating interfacial recombination by passivating the traps leads to a significant increase in PCE by 40% compared to reference devices[78].

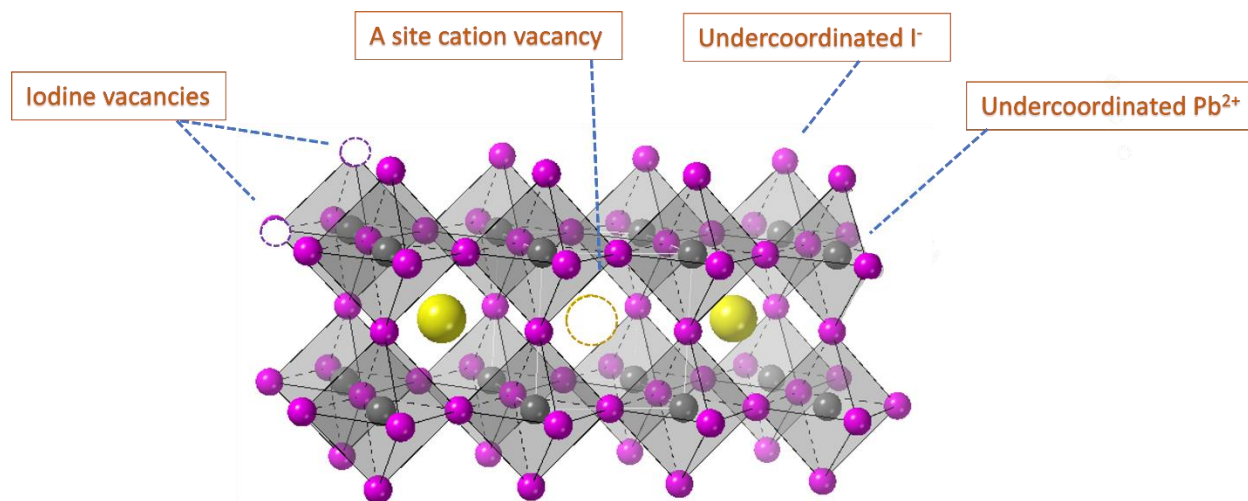


Figure 2.8 Common surface defects in lead halide perovskite thin films

Second, interfaces determine whether the photogenerated carriers generated in the perovskite can be smoothly transferred to the electron and hole transport layers. Energy band alignment between perovskite and CTL is crucial as band mismatch can lead to carrier accumulation and recombination at the interface, affecting the V_{OC} . Thus, interface treatment helps optimize charge extraction and transport. Qiu et al demonstrated the use of an aromatic group functionalized polymer at the perovskite/ TiO_2 ETL interface and found that interface engineering stabilized the device performance for over 250 hours of continuous operation in dry N_2 environment[14].

Third, the instability issue of perovskite layer in humid environments has been addressed using interface treatment strategy. Wang et al demonstrated the use of an amphiphilic block copolymer to suppress moisture and heat induced degradation of perovskite by passivating the grain boundaries where moisture can penetrate the perovskite, or volatile decomposition products can escape, accelerating perovskite degradation. Through interface optimization, flexible planar PSC with PCE of 21% was achieved[79].

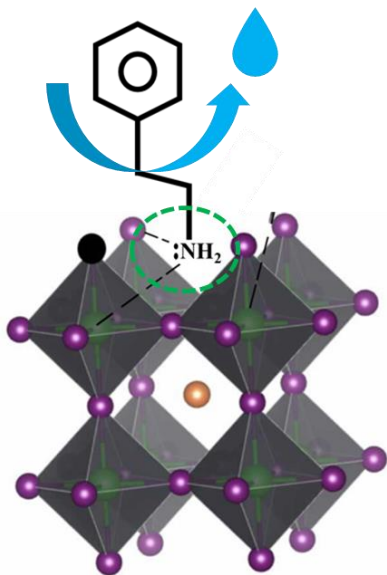


Figure 2.9 Bulky organic cations such as phenethylammonium iodide (PEAI) form a protective barrier over perovskite surface for moisture resistance.

Finally, interface engineering can help tackle challenges related to lattice strain in perovskite films[80]. Strain, or the deformation resulting from compression or expansion in the perovskite film, is caused due to the CTE mismatch between perovskite and the substrate. This is an artifact of annealing the perovskite film at high temperatures and its subsequent cooling, which causes volume expansion and shrinkage in perovskite and the substrate to different degrees. In addition, external influences such as light, heat or bias, which lead to ion migration, can also

produce microstrain during PSC operation[81]. Residual strain in perovskite films has been reported to lead to perovskite instability, increased defect density at the strained interfaces and eventual cracking or delamination, which also makes the perovskite prone to external degradation.[66, 68, 80] Lattice distortion can also trigger phase transformations at strained interfaces[82]. To resolve these, interface treatment has been employed with agents such as Ethyl p-nitrobenzoate (EPN), alkyltrimethoxysilane derivatives, ammonium formate, C=O functionalized adamantane derivatives in addition to many others, to act as a buffer strain release layer and help regulate residual strain[83-85].

Thus, it is clear that interfaces can be a key limiting factor in enhancing solar cell efficiencies, and adopting interface engineering approaches has multi-faceted benefits on both device stability and performance. One of the popular strategies explored in literature to eliminate interface defects is steric engineering by use of bulky organic passivating agents, among which aromatic amines offer some unique advantages[36, 41]. These include their high hydrophobicity as well as better charge transport brought on by the conjugated structure. Several recent works report on Sulphur functionalized organics such as thiophene to attain the synergistic effect of defect passivation and carrier transport [86, 87]. First, the presence of aromatic rings allows for charge delocalization due to conjugation, leading to high carrier mobility. Thiophenes further facilitate charge transport on account of their high polarizability as well as strong π - π and S-S interactions[88]. Second, their passivation mechanism relies on anchoring of the ammonia functional group in the molecule on to the surface of the perovskite to form a dense layer through ionic and hydrogen bonds. The ammonium functional group allows interactions between the nitrogen and lead halide octahedra in the perovskite through hydrogen bonds between NH_3^+ and I⁻ or coordinate bonds between N and lead ion interstitials (Pb^{2+}), leading to stabilization of the

corner-sharing $[\text{PbX}_6]^{4-}$ octahedral framework.[89-91] Third, the presence of Sulphur further links the organic cations with the perovskite by forming coordination bonds between the lone pair of electrons on Sulphur with the electron deficient Pb^{2+} . All these interactions serve to suppress undercoordinated $\text{Pb}^{2+}/\text{Pb}^0$ defects and iodide ion (I^-) vacancies. Finally, the aromatic part in the cations also forms a hydrophobic layer which serves to prevent moisture ingress in the perovskite and thus protect it from degradation.

While it's clear that these cations help passivate the surface defects, potentially detrimental interfacial changes arise when these passivated films are thermally stressed, offsetting their benefits. [21-23]. Under the high external temperatures in which solar cells operate, organic cations mobilize and tend to penetrate deep into the 3D perovskite structure, leading to reconstruction of the perovskite surface to lower dimensionality phases[18]. Consequently, the pristine perovskite structure responsible for current flow is now disrupted by these non-conductive molecules. These changes are detrimental to stable performances by affecting conductivity between perovskite and charge transport layers, introducing new charge trapping defects and changing the efficacy of defect passivation. Perini et al. investigated the effect of 200 hours of thermal stress on devices treated with passivation layers and report drops in current and voltage in passivated devices[92]. Under annealing, the organic molecule can diffuse into the perovskite lattice and replace the FA/MA cations, resulting in the formation of a lower dimensional 2D phase on top of the 3D perovskite films. Despite some existing literature[19], a more comprehensive

analysis is required to fully understand heat induced charge dynamics at passivated interfaces and the effect of 2D systems on charge transport and open circuit voltages in devices.

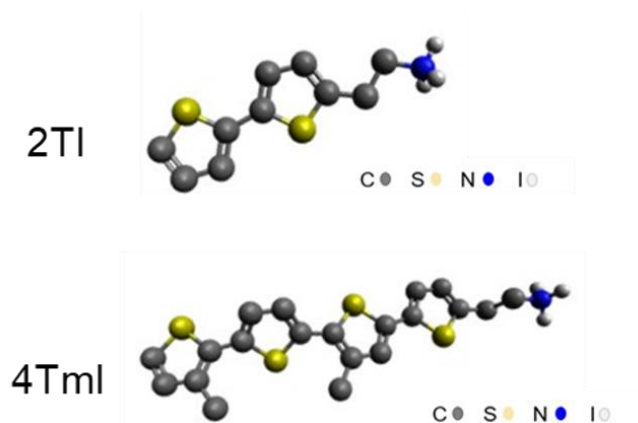


Figure 2.10 Long chain conjugated ammonium ligands used in this work.

In this work, conjugated ligands 2TI and 4TmI, with two and four thiophene rings respectively, as depicted in Figure 2.10 are used. They can anchor on to the surface of the perovskite through ionic and hydrogen bonds via their ammonium functional groups[91]. In addition, 2TI and 4TmI offer an energy band alignment suitable for hole transfer from the perovskite film to the hole transport layer[93]. Using different molecules allows for identification of structure induced molecular behavior, providing guidelines for design and selection of suitable passivation agents.

CHAPTER 3. EXPERIMENTAL METHODS

3.1 Perovskite Solar Cell and Thin Film Fabrication

Solar cells with direct n-i-p architecture were prepared on 1in x 1in patterned FTO glass substrate using solution-based method. The substrates were sequentially sonicated in a 2% Hellmanex solution, DI water, Acetone, and IPA for 20 min each, followed by drying with Nitrogen gun and placing on a hotplate. Glass slides were used to cover the edges of the substrates, leaving the active area exposed. An electron transport layer (ETL) consisting of a compact layer of TiO₂ was then deposited at 450°C through spray pyrolysis with 3.5 L min⁻¹ flow of oxygen carrier gas. The compact TiO₂ solution was prepared by mixing 0.480mL of Acetylacetone, 0.720mL of titanium diisopropoxide bis(acetylacetonate) (75% in 2-propanol) diluted in 10.8mL of pure ethanol. The solution was sprayed using a Sparmax spray gun in 10-15 second back and forth passages, with a 30 second delay between cycles which continued until the entire solution was utilized. The substrates were annealed at 450°C for an additional 30 min before being allowed cooling down to room temperature. This was followed by spincoating 60 μL mesoporous TiO₂ solution prepared by dissolving 150mg/mL titanium dioxide paste in ethanol (99.9 % pure, anhydrous from Sigma-Aldrich), at 4000rpm for 10 seconds, followed by annealing at 100C for 20 min. The substrates edges during spincoating were covered with magic tape to prevent TiO₂ deposition. The substrates were then sintered at temperature starting at 450°C and ramping down to 150°C, before being transferred to glovebox with <10 ppm O₂ and H₂O. on top of the ETL, 60 μL of 1.24M Cs_{0.05}FA_{0.95}PbI₃ perovskite solution was spincoated at 1000 rpm for 10 s, followed by 6000 rpm for 20 s. 250 μL of Chlorobenzene (Sigma-Aldrich, anhydrous) was dropped at 26 s from the start of the spincoating recipe. The devices were then annealed at 150°C for 20 min. For top passivation, 80 μL each of either 1.35 mg/mL 2TI or 2.12mg/mL 4TmI (4mM solution for

both cations) dissolved in Isopropyl alcohol (anhydrous – Sigma-Aldrich) was dynamically spin coated on top of the perovskite film at 5000rpm, 5000rpm/s, 20s. The films were then annealed at 100°C for either 10 or 40 min. For depositing the hole transport layer (HTL), 0.07M solution of Spiro-OMeTAD powder dissolved in chlorobenzene was mixed with 67.06 μ L tert-butylpyridine (TBP- SigmaAldrich), 30 μ L of 1.8M Li-TFSI (Sigma- 3 Aldrich in acetonitrile anhydrous) and 16.64 μ L of 0.25M Co(II) salt (FK209 - Sigma-Aldrich in acetonitrile anhydrous), in that order. 90 μ L of this solution was dynamically spincoated at 1-2 seconds after start at 3000rpm, 3000rpm/s for 20 seconds. The CsFA and Spiro-OMeTAD films were cleaned off the substrate edges using dimethylformamide and then acetonitrile. Finally, 43 nm thick Au top electrode gold electrode was thermally evaporated on top of the HTL.

3.2 Compositional and Structural Characterizations on Films

3.2.1 X-ray Photoelectron Spectroscopy

X-ray Photoelectron Spectroscopy (XPS) was performed on perovskite films deposited on FTO substrates and used to verify the presence of passivating cations and to observe changes in surface composition upon thermal exposure. XPS survey scans were obtained using a Thermo Scientific K Alpha X-ray Photoelectron Spectrometer using the Cu $K\alpha$. It is a surface sensitive technique which probes the top 1-10 nm of the material[94]. The measurement relies on irradiating a sample surface with a focused beam of X rays in vacuum. This leads to emission of electrons from the near surface region by photoelectric effect. Ejected electrons are collected, and a spectrum is recorded by plotting the counts of electrons as a function of their kinetic energies. The intensity and position of the obtained peaks gives information about the elements that the electrons were bound to and their chemical environment.

For the measurements presented in the following chapter, scan parameters were 200eV pass energy and 1eV energy step; elemental scan parameters were 50eV pass energy and 0.1eV energy step. Profiles were obtained for Pb 4f (5 scans), I 3d (5 scans), C 1s (20 scans), N 1s (10 scans) and S 2p (10 scans). Thermo Scientific Avantage software was used to perform surface analysis from the data; the Pb-X peak position was used as the reference to perform binding energy shift for all samples. A typical XPS pattern of Pb 4f is shown in Figure 3.1.

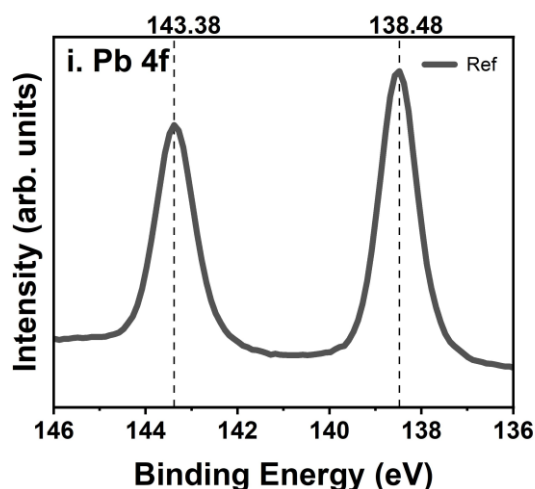


Figure 3.1 A typical XPS spectra for Pb 4f obtained from CsFAPbI₃ thin film.

3.2.2 Scanning Electron Microscopy

Scanning Electron Microscopy (SEM) was performed to obtain the surface morphology of control and passivated perovskite films. SEM images were obtained with a Hitachi SU8230 secondary electron detector to determine the film morphology at an accelerating voltage of 3.5kV and current of 10 μ A. To obtain good electrical conductivity and achieve well resolved images, carbon tape was used to connect all film samples to the sample stub. A typical SEM image of perovskite film surface (control sample) is shown in Figure 3.2.

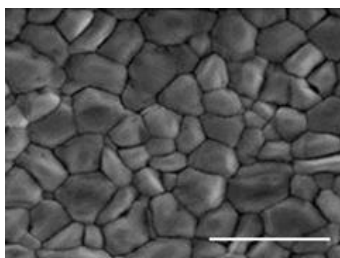


Figure 3.2 A typical surface SEM image of CsFAPbI₃ film. Scale bar is 1 μ m.

3.2.3 Grazing Incidence Wide Angle X-ray Scattering

Grazing Incidence Wide Angle X-ray Scattering (GIWAXS) measurements were performed on perovskite/passivation films deposited on FTO glass substrates to understand the crystalline features and dimensionality of the deposited films. This technique works by irradiating the sample with X-rays at low enough incidence angles to just graze the thin film surface. Incidence angles can be varied to change the penetration depth of the X rays, allowing examination of structural evolution at the surface versus bulk regions of the perovskite.

GIWAXS images were taken on 0.5 x 0.5 sized samples at the National Synchrotron Light Synchrotron II at Brookhaven National Laboratory. X-ray beam with energy 13.5 keV, 1mrad divergence and resolution 0.7 % was used to obtain images at incidence angles of 0.1° and 0.5° (for surface versus bulk structures respectively) with an exposure time 20s. SciAnalysis software package was used for data analysis. Sector averages were taken along $\pm 20^\circ$ from the vertical to enhance the signal from low dimensional phases formed at the interface. A typical GIWAXS pattern of CsFAPbI₃ film is indexed and shown in Figure 3.3.

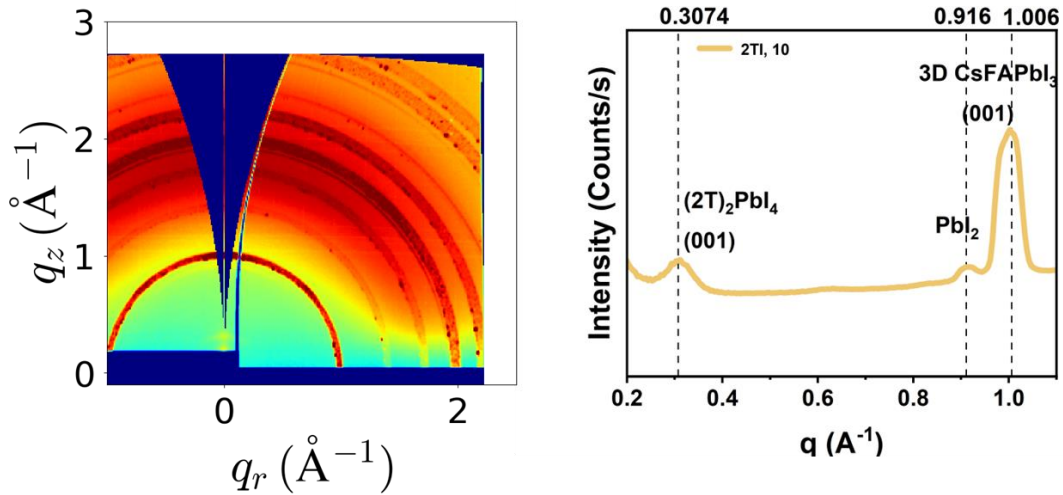


Figure 3.3 A typical GIWAXS 2D pattern (left) and intensity profile (right) for 2TI passivated perovskite film annealed for 10 minutes at 100°C.

3.3 Optical Characterizations

3.3.1 X-ray excited optical luminescence

X-ray excited optical luminescence (XEOL) measurements were performed on complete solar cell stack *fluorine tin oxide (FTO) / compact-TiO₂ / mesoporous-TiO₂ ETL / Cs_{0.05}FA_{0.95}PbI₃ perovskite / 2TI or 4TmI passivation / Spiro-OMeTAD HTL / gold top contact*. The long penetration depth of X-rays allow probing local electronic properties of the modified perovskite surfaces. A schematic diagram shown in Figure 3.4 represents the generation of electrons and holes upon absorption of X rays. These charge carriers can subsequently recombine radiatively to emit photons, resulting in an intensity of emission that can be spatially mapped over the observed film area.

Perovskite solar cells were investigated with a 250 nm full-width-half-maximum (FWHM) focused beam at 14 keV in a home-built in-situ cell. The XEOL signal was collected using a

Mitutoyo 20X microscope objective through the FTO/glass substrate. This signal was subsequently guided to a spectrometer (Horiba) equipped with a spectroscopic electron multiplying CCD (EMCCD, Andor Newton) charge-coupled device detector (Andor). An area of 80x80 pixels with each pixel being 0.3 μm in step size was analyzed and the intensity was integrated between 1.5 and 1.6 eV at each point.

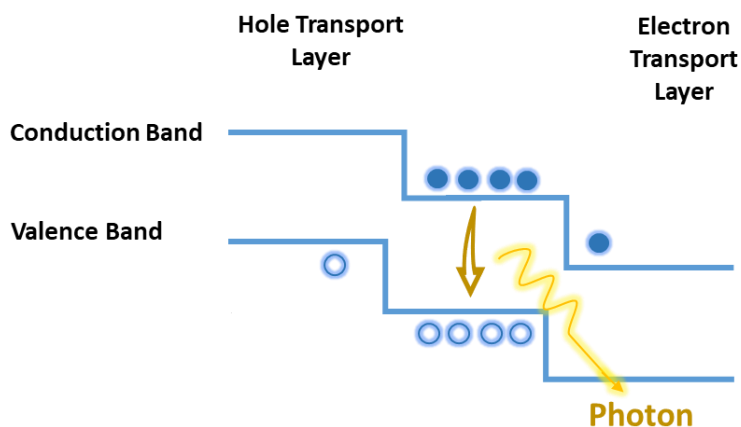


Figure 3.4 Mechanism of X-ray excited optical luminescence

3.4 Electrical Characterization

3.4.1 X-ray beam induced current

X-ray beam induced current (XBIC) measurements were performed simultaneously with the previously explained XEOL measurements. As before, perovskite solar cell devices with architecture *fluorine tin oxide (FTO) /compact-TiO₂/mesoporous-TiO₂ ETL/ Cs_{0.05}FA_{0.95}PbI₃ perovskite/ 2TI or 4TmI passivation/Spiro-OMeTAD HTL/ gold top contact* were examined with 250 nm full-width-half-maximum (FWHM) focused beam at 14 keV. A schematic diagram is shown in Figure 3.5. With the absorption of X Rays, electrons and holes are produced. Instead of recombining as in XEOL, these charge carriers can be extracted by charge selective electron and

hole transport layers and collected at contacts to obtain localized current values at each spatial point. The device is connected in short-circuit condition and the induced current is amplified using an SR570 current amplifier.

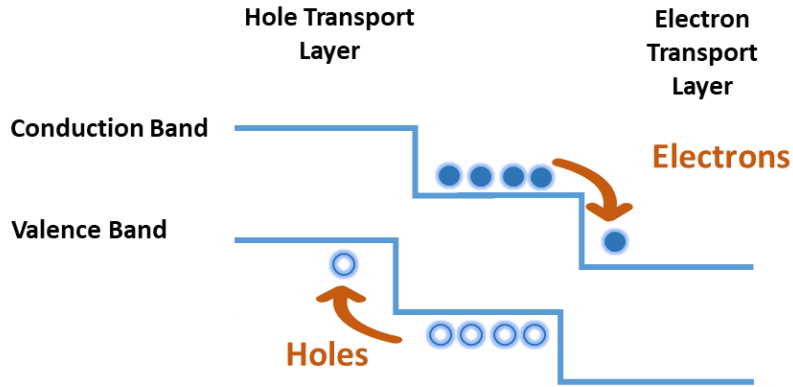


Figure 3.5 Mechanism of X-ray beam induced current. Instead of recombining, the charge carriers are extracted by charge selective electron and hole transport layers.

3.4.2 Kelvin Probe Force Microscopy

Kelvin probe force microscopy (KPFM) measurements were performed to obtain the Contact Potential Difference (CPD) of the pristine and surface treated films in which the electrostatic force between the AFM tip and the sample is minimized[95]. The CPD is defined as $CPD = \Phi_{tip} - \Phi_{sample}$ and is measured at each scan point by applying a DC voltage V_{dc} to compensate for the work function difference.

To understand the results of KPFM, it is important to understand the mechanisms behind band bending in semiconductors[96]. The surface of a semiconductor contains dangling bonds with unpaired electrons which interact with each other and form a surface electronic state at the semiconductor bandgap. Usually, surface states have a much higher density than the bulk dopant states and end up pinning the fermi level at a different energy position compared to the bulk. In an

intrinsic semiconductor, in the absence of charge transfer between bulk and surface, the fermi level of the bulk and of the surface are aligned and flat. In doped semiconductors, depending on the type of doping, the fermi level of the bulk is either higher or lower than the fermi level of the surface states. This means that electrons transfer from either bulk to the surface (in n-type) or from surface to the bulk (in p-type). This charge transfer continues to the point of equilibrium where the fermi levels of both the surface and bulk are aligned, causing a bending in the CB and VB. This bending is either upward or downward, depending on the nature of excess charges near the surface. The surface states are determined by the atomic structure of the semiconductor, and depending on the surface treatment, the surface state induced band bending can change.

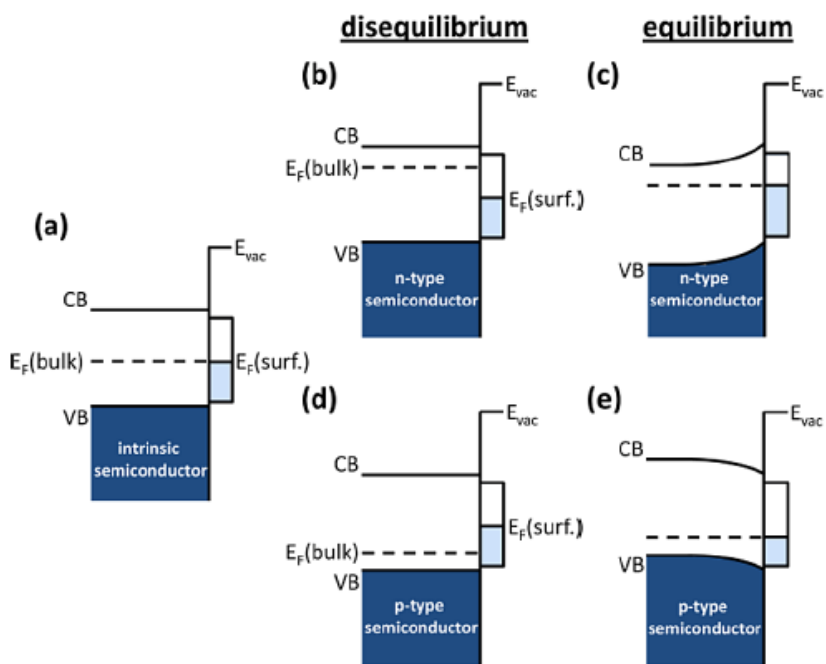


Figure 3.6 Schematic of electron energy levels near the surface of a clean semiconductor: (a) intrinsic semiconductor; (b) disequilibrium and (c) equilibrium between n-type bulk and its surface; (d) disequilibrium and (e) equilibrium between p-type bulk. Reprinted with permission from [96] Copyright 2012 American Chemical Society.

Under illumination, photons with energy larger than bandgap generate electrons-holes pairs in the semiconductor. These charge carriers distribute throughout the material, electrons and holes moving in different directions under the influence of an electric field in the bent band region. For example, for an n-type semiconductor with upward bent bands, the surface is electron rich surface. Free holes go towards surface and neutralize the accumulated excess negative charges, causing the band edges to partially flatten. The SPV is a measure of the potential difference created at the surface due to the presence of these excess charge carriers and is determined by measuring the difference in surface potential under dark versus under illumination, $SPV = V_{\text{illumination}} - V_{\text{dark}}$. Alternatively, SPV can be understood as the degree of band flattening produced upon illumination. The sign and magnitude of SPV provide insights into near surface band bending, which can be related to the p- or n-type nature of a material.

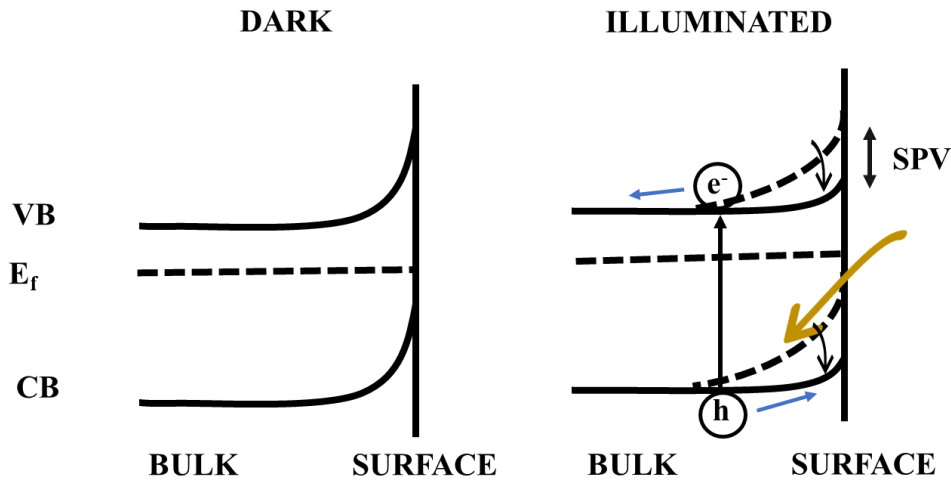


Figure 3.7 Band flattening observed as surface photovoltage measurements using kelvin probe force microscopy technique.

3.4.3 Current Density-Voltage Characteristics (J-V)

A solar cell device's performance characteristics are assessed by extracting information from a current density-voltage (J-V) curve. This curve is obtained by conducting a voltage sweep in both the reverse and forward directions, resulting in a current density for each corresponding voltage point. The J-V measurements are conducted under both illuminated and dark conditions. Typically, the device is irradiated with one sun (100 mW/cm^2 , AM 1.5G) with a solar simulator that can also adjust light intensity and tune the light spectrum. From the resulting J-V curve, it is possible to calculate key solar cell parameters, including short-circuit current (J_{sc}), open-circuit voltage (V_{oc}), fill factor (FF), maximum power point (MPP), and power conversion efficiency (PCE). The fill factor is determined as the ratio between the MPP, and the power derived from $J_{sc} \cdot V_{oc}$. The PCE, expressed as a percentage, is computed by comparing the MPP to the incoming solar power (100 mW/cm^2).

In this work, J-V characteristics of perovskite solar cells were obtained using a Fluxim Litos Lite setup enabled with Wavelabs Sinus- 70 AAA solar simulator with standard air mass 1.5 global (AM 1.5G) illumination at room temperature and Nitrogen flow in the chamber. Forward and reverse J-V scans were collected in the range 1.2 to -0.5 at 50mV/s scan rate, and stabilized power output was collected with maximum power point tracking for 60s. Masks were placed over the device to define an active pixel area of 0.0625 cm^2 .

CHAPTER 4. STERIC ENGINEERING CONTROLLED STABILITY OF CSFAPBI₃ INTERFACES

4.1 Introduction

A major commercialization bottleneck in perovskite photovoltaics is the instability of the perovskite material in ambient conditions. This instability can arise due to an attack of moisture or oxygen and is exacerbated in the high external temperatures at which solar cells operate. Devices that have been aged over long time periods also show worsening hysteresis because of ion movement from the perovskite bulk to the surface[97]. Interfaces are also particularly prone to formation of point defects which can act as traps to attract charge carriers and impact device performance.

All these factors call for the use of novel interface engineering techniques that can not only passivate the defects, but also render devices stable under long operational lifetime. Up-and-coming passivation agents such as thiophenes show promising trends for defect passivation but as discussed in Chapter 2, thermal stability in these passivation layers is challenging due to formation of low dimensional phases. While on one hand, these 2D layers consisting of bulky organic spacer cations exhibit high hydrophobicity and impede ion migration related hysteresis effects in 3D perovskites[35, 98, 99], on the other hand, their insulating character poses problems when it comes to conductivity and charge extraction in perovskite films[100, 101]. Thus, the goal is to find the right balance to combine the advantages of both 3D and lower dimensional perovskites for superior stability and performance.

In the first phase of the work, perovskite films are passivated with molecules of different sizes and annealed for different durations. This has two major outcomes. First, it is aimed at investigating how the perovskite surface evolves with heating. By observing the appearance of

hybrid perovskite phases in synchrotron-based angle dependent GIWAXS, it is possible to identify perovskite-molecule interactions and resulting structural changes. Second, use of two different ligands with the same ammonium head groups but different backbone lengths allow for exploration of steric effects. Steric hinderance has been shown to directly affect tolerance factor, phase stability, trap passivation efficacy and optical bandgap in perovskite materials[102-104]. This correlation is significant because molecular size directly affects mobility of the molecules, uniformity of passivation layer, and the likelihood of triggering structural changes[105]. Overall, this chapter will highlight the formation of surface treatment layer and will discuss its morphology, compositional and structural changes under thermal annealing.

4.2 Results and Discussion

4.2.1 Surface morphology change

Scanning electron microscopy (SEM) was performed to observe the differences in surface morphology before and after cation treatment and to contrast the evolution of 2TI versus 4TmI on annealing (including reference films). The images in Figure 4.1 indicate that surface morphology is preserved after treatment with 2TI, while treatment with 4TmI leads to formation of aggregates of the salt. These clusters are attributed to strong inter-molecular interactions in the larger sized 4T cations. The aggregates weaken and decrease in size with prolonged thermal stress. The aggregates can be seen disappearing upon annealing for 40 min, suggesting their diffusion to form a layer over the perovskite film.

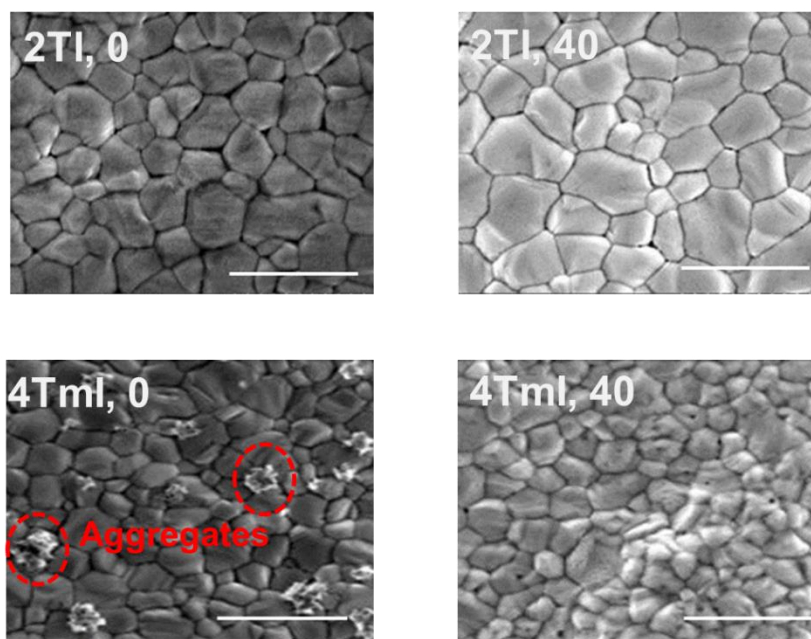


Figure 4.1 Film morphology seen in SEM images for 2TI- 0; 2TI-40 and 4TmI-0; 4TmI-40 films. 0 and 40 are annealing times at 100C. Scale bar is 1 μ m.

4.2.2 Surface chemistry change

To further verify the deposition of this surface passivation layer as well as the compositional changes at the interface, surface sensitive X-ray photoelectron spectroscopy (XPS) measurements were performed on the reference and the surface modified CsFA films at different annealing times. The elemental scans for N 1s and Pb 4f are presented in Figure 4.2. The remaining C 1s, S2p, and I 3d elemental scans are reported in Figures A3 and A4 for completeness. For both ligands, the presence of the S 2p signal confirms that the capping layer is indeed present at the top surface. The intensities of Pb 4f signals in the XPS scans provide important insights into the diffusion behavior of cations under heat. In both cases of as deposited 2TI and 4TmI films (i.e. 2TI- 0 and 4TmI-0) the Pb peak at 138.48 eV is suppressed compared to the reference due to the

shielding of Pb signal by the cations deposited over the perovskite film. Upon annealing at 100°C for 40 min, the Pb 4f peak intensity increases for 2TI, while it decreases for 4TmI.

In the N 1s scans in Figure 4.2, the intensity of the N=C peaks at 400.68 eV - corresponding to formamidinium (FA) - decreases as passivating molecules are added atop the perovskite layer because of FA getting covered by the other cations. Contemporarily, a new peak appears at 402.68 eV, from the N-C bond in 2T and 4TmI. Upon annealing for 40 min, the N=C signal increases in 2TI, and decreases in 4TmI, with the N-C signal following the opposite trend in the two films. The surface changes are completed within 10 min for the 2T⁺ cation, while they keep progressing in 4Tm⁺ treated films. These results can be understood in terms of cation diffusion. 2T⁺, the smaller of the two ligands, penetrates the bulk of the 3D film more rapidly via grain boundaries, and completes the structural changes at the interface within the first 10 min of annealing. The bulkier 4Tm⁺ cations instead require more energy to separate from the aggregates and spread on the surface. By observing the opposite trend in N 1s and Pb 4f peaks in 2TI and 4TmI, the hypothesis is that 2T⁺ immediately reacts with the surface, diffusing at grain boundaries, while 4Tm⁺ remains limited at the surface of the perovskite film creating a very uniform capping layer.

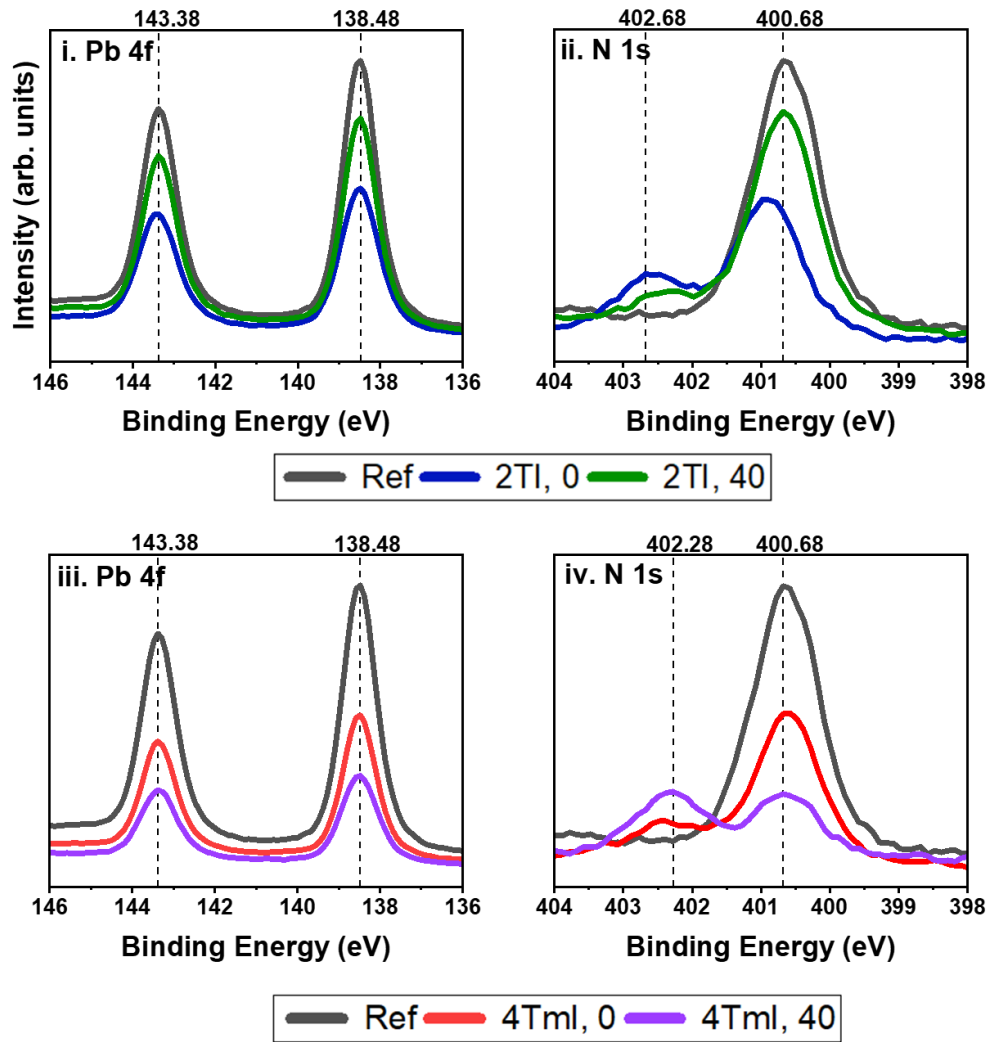


Figure 4.2 XPS spectra for Pb 4f and N 1s for reference (black) versus passivated films-2TI (top) and 4TmI (bottom).

4.2.3 Surface versus bulk crystal structure

To correlate the compositional changes at the surface with structural information, Grazing Incidence Wide Angle X-ray Scattering (GIWAXS) measurements were performed at an incidence angle of 0.1° [106]. The sector averages taken along $\pm 20^\circ$ from the vertical are presented in Figure 4.3 to enhance the signal from low dimensional phases formed at the interface.

Comparison of the GIWAXS patterns for 2TI/4TmI treated interfaces with the pristine perovskite film reveals the presence of peaks at low angles that can be attributed to low dimensional Ruddlesden Popper phases. In Figure 4.3(left), the intensity profiles of the 2TI films reveal a weak signal at $q = 0.3 \text{ \AA}^{-1}$ corresponding to the $(2T)_2\text{PbI}_4$ phase identified by Dou et al[93]. The peak appears first after 10 min of thermal treatment and remains upon prolonged annealing for 40 min. In 4TmI treated interfaces, a peak is visible at $q = 0.44 \text{ \AA}^{-1}$. Before annealing, ascribed to the pure 4TmI cations and consistent with the presence of aggregates at the surface of the film as observed by SEM. Only after 40 min of annealing are the two new peaks observed at $q = 0.38 \text{ \AA}^{-1}$ and 0.59 \AA^{-1} , which belong to the (400) and (600) of the $(4Tm)_2\text{PbI}_4$ phase[93]. The fact that a longer annealing is necessary to trigger conversion of 4TmI to a Ruddlesden-Popper phase is consistent with the observations both by SEM and XPS.

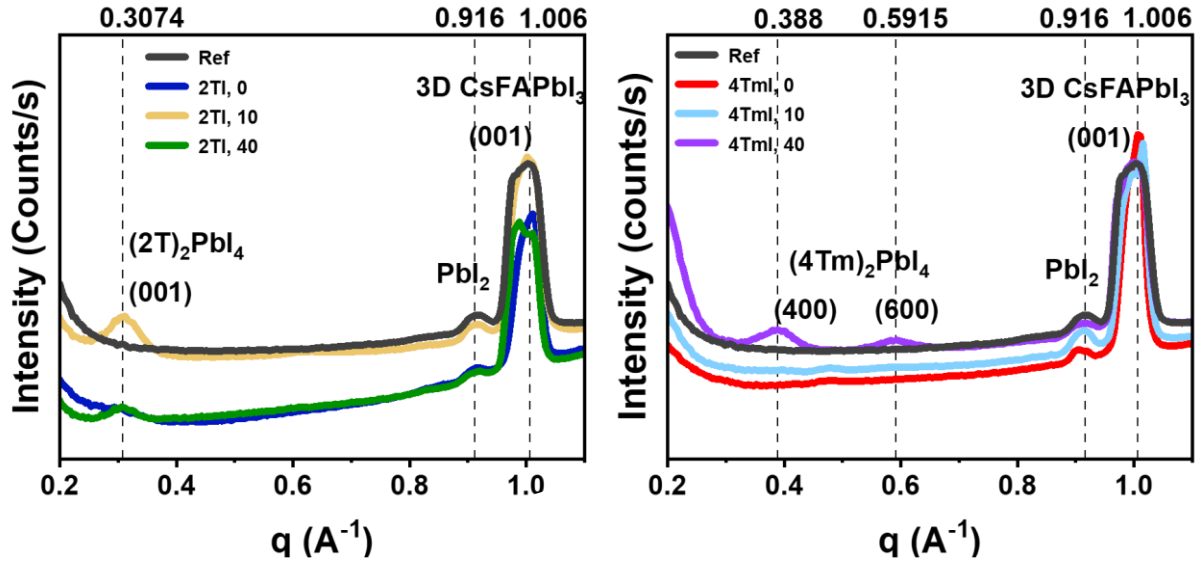


Figure 4.3 GIWAXS intensity profiles comparing reference perovskite with 2TI (left) and 4TmI (right) passivated films.

4.2.4 DFT Simulation of cation binding energy

Computational analysis has been used in literature to study the internal interactions between bulky cations and the inorganic perovskite network and has been shown as an effective tool in predicting the stability of perovskite structures[91, 107]. The incorporation of large sized cations into the lattice affects the degree of octahedral tiling, DFT calculations on cation binding energy have implications on stability of the perovskite structure[41]. To study the strength of the interaction of $2T^+$ and $4TmI^+$ cation with the perovskite surface, the strength of interaction of a monolayer of these cations with the perovskite surface was simulated. The DFT result presented in Figure 4.4 highlights a stronger interaction of $4Tm^+$ cations with the surface compared to $2T^+$. As the head groups in $2T^+$ and $4Tm^+$ are the same, the difference is ascribed to the stronger π - π stacking of $4Tm^+$ cations, which stabilizes a continuous $4Tm^+$ film at the surface.

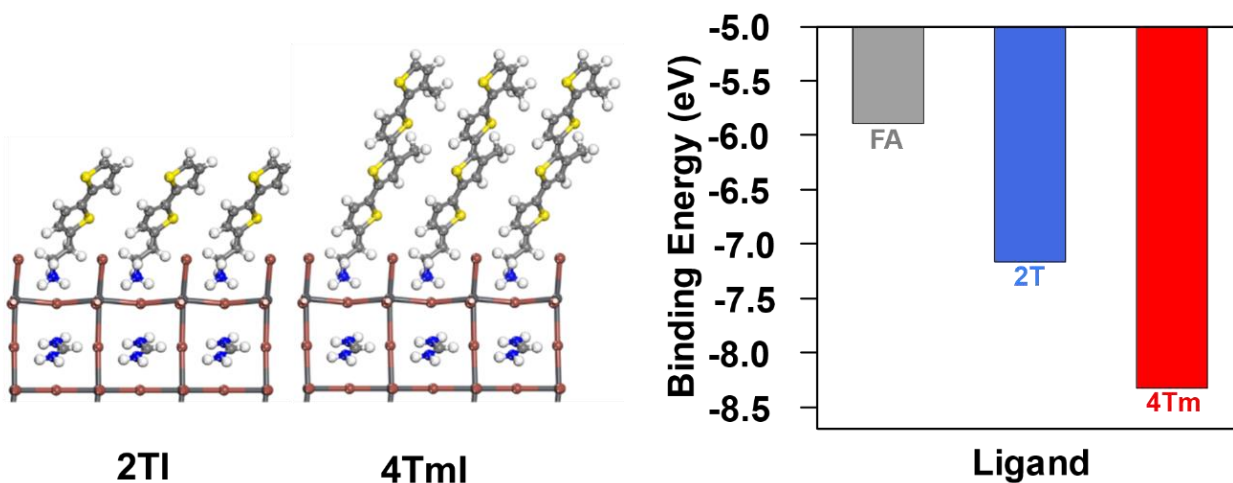


Figure 4.4 DFT Computations: Ligand anchoring (left) and binding energy with the PbI_6 sub lattice (right).

4.3 Conclusion

The important role of steric hinderance in passivating and stabilizing perovskite interfaces has been discussed in previous reports, which have provided evidence that bulky cations can induce instabilities in the three-dimensional perovskite network, leading to formation of two-dimensional phases with the perovskite under external stressors. This chapter focuses on the evolution of passivated perovskite interfaces on heating and specifically explores the differences originating from use of passivated cations of different steric sizes.

The data presented on morphology, composition and structural characterization indicates that steric size of organic molecules controls the rate of structural changes. Evolution of 2TI and 4TmI surface treatment layers occurs with annealing as follows: Within the first 10 minutes of annealing, 2TI undergoes conversion to $n=1$ R-P phase which persists after annealing for 40 min. On the other hand, 4TmI on account of its larger bulk, exhibits slower diffusion kinetics, resulting in the delayed formation of $n=1$ R-P layer which becomes apparent only after 40 min annealing. The divergence in hole extraction behavior for the two cations is due to their distinct binding energies which consequently impact the uniformity and homogeneity of coverage in these insulating 2D layers. From our computational results, 4TmI, the bigger of the two cations is more strongly bound to the perovskite surface than 2TI, meaning that 2TI would be more prone to leaving behind vacancies even under short thermal exposure. These vacant 2TI sites could potentially become direct points of contact between perovskite and the hole transport layer, enabling faster hole extraction without the hinderance due to 2D organic layer. The length of this organic barrier also depends on the size of the backbone, and is expected to be shorter for 2TI, with two thiophene rings, than 4TmI with four thiophene rings in the out of plane direction. This will have implications for charge extraction and current generation from passivated films and is

discussed in detail chapter 5. A schematic of time dependent thermal diffusion behavior differing for the two ligands, 2TI and 4TmI is depicted in Figure 4.5.

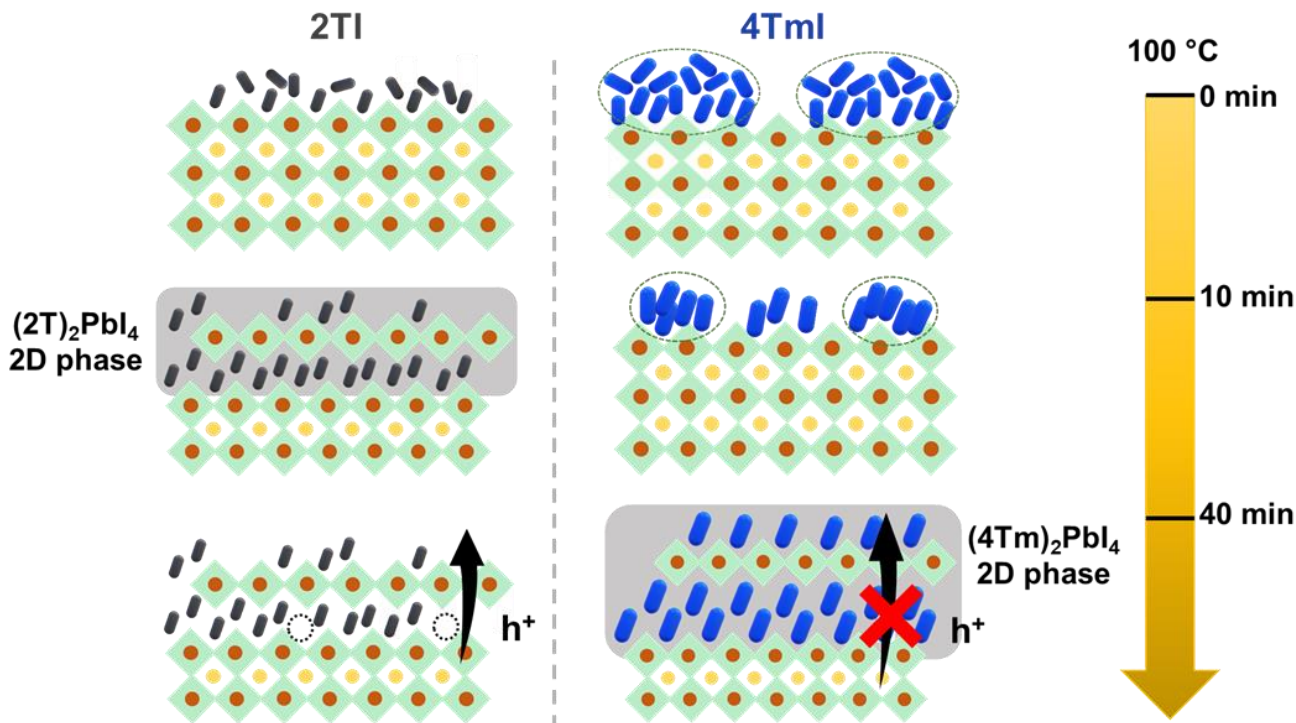


Figure 4.5 Mechanism of heat induced diffusion in 2TI versus 4TmI. 2TI undergoes conversion to n=1 2D phase within the first 10 mins of annealing, while 4TmI has slower diffusion kinetics, resulting in a homogeneous n=1 2D spacer layer only after annealing for 40 min.

CHAPTER 5. INFLUENCE OF CAPPING LAYER ON CHARGE EXTRACTION IN PEROVSKITE SOLAR CELLS

5.1 Introduction

Chapter 4 discussed the formation of lower dimensional perovskite layers formed under thermal annealing of the passivation cations. Generally, replacing 3D perovskite in the active layer with 2D counterparts is undesirable as 2D perovskites show limited photoconversion efficiencies due to narrow solar absorption range, poor charge transport, and large exciton binding energies[101, 108]. Lower dimensional perovskite (LDP) systems consist of n number of perovskite octahedra sheets ordered periodically and sandwiched between organic layers. These systems exhibit quantum confinement behavior- organic cations templating the inorganic perovskite network have small dielectric constant and act as a “barrier”, whereas the inorganic sheets with a higher dielectric constant act as “wells”.

From a device perspective, quantum confinement effects in LDPs lead to important considerations in optoelectronic properties. Due to the insulating spacer later formed of intercalating cations, the out-of-plane conductivity in 2D perovskite systems such as R-P, is severely restricted[108]. This hinders charge transport perpendicular to the planes while causing charge accumulation and recombination in PSCs. Numerous studies have demonstrated that controlling the packing and orientation of spacer cations in 2D perovskite layers can help maximize charge transport in the vertical direction[100, 109-111]. In addition, tailoring interlayer spacing between inorganic layers helps tune the bandgap and thus optoelectronic properties in LDPs[111-113]. The size and nature of organic cations can significantly affect both their orientation and layer spacings, and manifest as differences in device performance.

The second phase of this work, covered in this chapter, turns to the consideration of device performances based on passivated films. This chapter will elucidate performance variations resulting from the correlation previously established between thermal stability of perovskite films and the structure/size of passivating molecules. Complete perovskite devices based on n-i-p architecture were fabricated using 2TI and 4TmI passivation layers and device-level characterizations were performed to understand optoelectronic behavior, surface potential variations and current-voltage characteristics. This chapter focuses on (1) localized carrier transport dynamics and undesired non-radiative recombination that allow the PCEs of passivated devices to exceed 20% and (2) the origin of improved device performance and the caveats.

5.2 Device Performance

5.2.1 Surface Photovoltage

To try to understand how passivation impacts surface potential, Kelvin probe force microscopy (KPFM) measurements were performed to obtain the Contact Potential Difference (CPD) of the pristine and surface treated films, by minimizing the electrostatic force between the AFM tip and the sample [95]. The CPD is defined as $CPD = \Phi_{tip} - \Phi_{sample}$ and is measured at each scan point by applying a DC voltage V_{dc} to compensate for the work function difference.

As shown in Figure A8, after passivation, the 2TI/4TmI treated films exhibit a heterogeneous voltage response compared to the untreated reference film. This suggests that the interfacial changes upon treatment with the organic layer manifest as spatial contact potential variations. As shown in Figure A11, passivation also results in smoother interface topography and lower mean square roughness of the films which likely promotes charge carrier extraction due to a better contact of the layer with the overlying HTL. The KPFM technique can be further employed to measure the surface photovoltage (SPV), which is defined as the difference in surface potential

under dark versus under illumination, $SPV = V_{\text{illumination}} - V_{\text{dark}}$. The sign and magnitude of SPV provide insights into near surface band bending, which can be related to the p- or n-type nature of a material. Based on the graph shown in Figure 5.1, the change in the sign of SPV from negative to positive for the untreated pristine film and treated perovskite films, respectively, indicates that the surface termination changes on passivation. Since the magnitude of SPV is essentially the degree of band flattening under illumination, the much higher absolute SPV value for 2TI, 0 compared to reference suggests that the potential barrier for the carriers to overcome (and transfer to HTL) is reduced for 2TI passivated devices, while the differences between SPV magnitude for 4TmI-passivated and reference devices are not as significant.

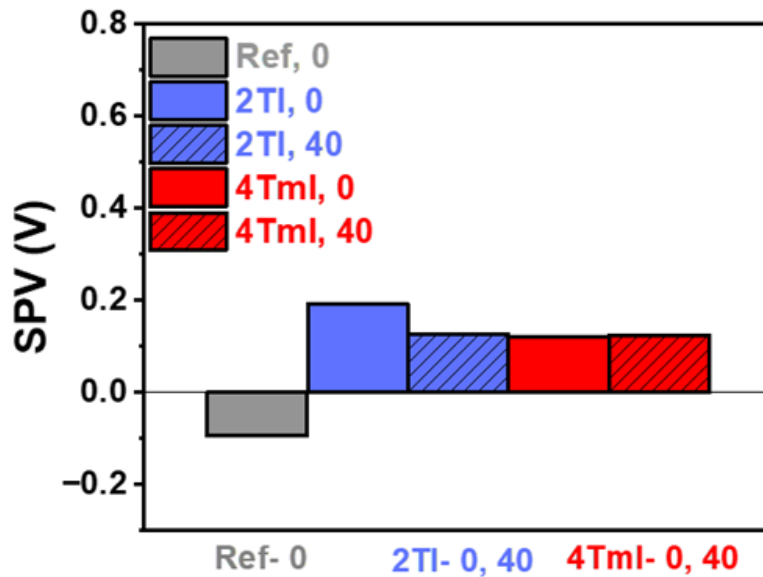


Figure 5.1 Surface Photovoltage histogram. For contact potential distributions showing potential spread and mean used for SPV (CPD_mean(light)- CPD_mean(dark)), refer to Figure A9

To understand how the interface energetics varies during thermal stress in surface treated films, potential response was compared from as-deposited films to films that had been annealed for 40 min at 100°C (CPD maps presented in Figure A9). From Figure 5.1, 2TI shows slight

potential changes upon annealing. Notably, KPFM measures the potential originating from only the material surface and annealing for 40 min reduces the surface concentration of 2TI as suggested by XPS. The observed signal thus presumably arises from a combination of the remaining 2TI ligands atop the perovskite as well as the underlying perovskite exposed due to heterogeneity in ligand distribution. On the other hand, the signal from 4TmI shows negligible variations on annealing, again underscoring the tendency of this ligand to stabilize on the surface due to limited mobility. Further, under prolonged heating, 4TmI molecules overcome the intermolecular attractive forces that keep them aggregated at the surface and spread over the perovskite film, increasing surface coverage. This shields the underlying perovskite signal, giving us a true representation of only the 4TmI voltage response. This spread is also clear from the CPD maps in Figure A8 with the low potential regions (seen as darker spots due to ligand clusters) homogenizing on the surface in both the dark and illuminated conditions.

5.2.2 Charge carrier dynamics

The change in surface band bending character on introducing the ligands suggests a further influence on the charge transfer mechanisms at the interface. To understand the charge carrier dynamics, X-ray beam induced current (XBIC) and X-ray excited optical luminescence (XEOL) experiments were performed on complete solar cells utilizing the long penetration depth of the incident X-rays to probe the local electronic properties of the perovskite layers after surface modification. The solar cells were realized using the stack fluorine tin oxide (FTO) /compact-TiO₂/mesoporous-TiO₂ ETL/ Cs_{0.05}FA_{0.95}PbI₃ perovskite/ 2TI or 4TmI passivation/Spiro-OMeTAD HTL/ gold top contact. Aged devices were selected to understand the long-term impact of perovskite surface modifications on device performances. Upon X-ray exposure, charge carriers are generated in the perovskite layer. After excitation, the charge carriers relax at the band edges

and can be either extracted as current in short-circuit condition (known as XBIC) or recombine and emit photons that can be collected as luminescence (known as XEOL). The simultaneous acquisition of XBIC and XEOL allows us to assess charge extraction efficacy from the device and charge recombination dynamics in the active layer with spatial correlation. The XBIC and XEOL maps of the films are presented in Figure 5.2.

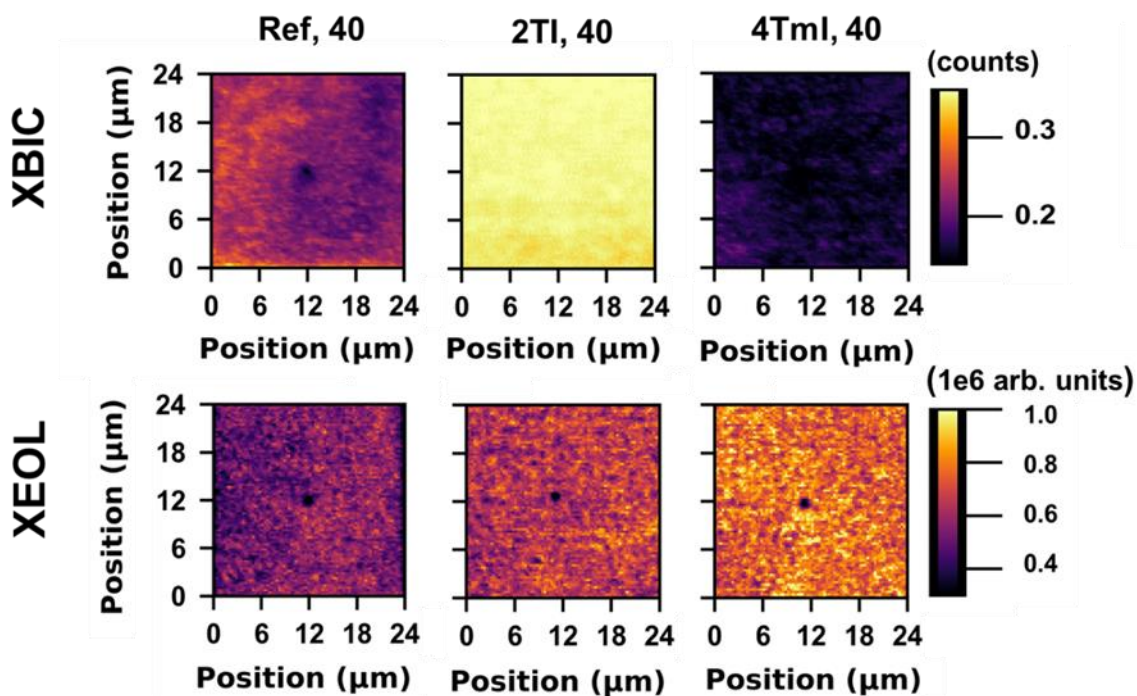


Figure 5.2 Charge extraction and recombination in Reference, 2TI and 4TmI films after 40 min annealing at 100 °C.

The XBIC maps show variations in the efficacy of charge extraction between the reference and devices including the surface treatment. The XEOL maps show the photoluminescence (PL) intensity from the films, integrated between 1.5 and 1.6 eV for each pixel. 2TI treated perovskite

films show an increase in extracted current upon X-ray exposure with respect to the reference, indicative of efficient hole extraction from the CsFA layer into the Spiro-OMeTAD HTL. The PL from 2T also increases with respect to the reference, as revealed by the XEOL maps. This can only be explained by effective passivation of defects, which reduces non-radiative recombination thus increasing contemporarily XEOL and XBIC signals. Contrary, 4TmI treated films reveal currents that are below the reference. Such a difference could be ascribed to the formation of a thicker and uniform film of $(4Tm)_2PbI_4$ at the interface with Spiro-OMeTAD, which impedes charge extraction. The decreased extraction efficacy contributes to the highest PL intensity measured for 4TmI treated films, compared to the 2TI treated- and untreated- perovskite samples. From these measurements, we can conclude that the organic spacer layer formed between the perovskite and the HTL has a great influence on carrier dynamics. Particularly, 2TmI passivates the surface of perovskite films while enabling efficient charge extraction and transport. 4TmI instead localizes at the interface between perovskite film and HTL, creating a barrier to charge extraction. Alternatively, the efficient charge extraction observed with 2TI could be ascribed to non-uniformities in the $(2T)_2PbI_4$ coverage. Spatial heterogeneity in annealed 2TI films is also notable from the dark areas previously seen in the contact potential maps obtained from KPFM in Figure A8, creating direct carrier transportation pathways between perovskite and HTL.

5.2.3 *J-V characteristics*

To determine whether the device performances are affected by the length of the oligothiophene tail in the conjugated molecules, batches of n-i-p planar heterojunction solar cells were fabricated with the architectures of FTO/TiO₂/CsFA perovskite/ passivation/Spiro-OMeTAD/Au, where the passivation layer was either none, 2TI, or 4TmI. Figure 5.3 presents a schematic of the reference solar cell along with box plots of device parameters (PCE, V_{OC} - open-

circuit voltage, J_{SC} -short-circuit current) for both passivated and pristine perovskite devices. Absolute values of these parameters are also summarized in Table 2.

The control device shows a mean PCE of 12.6% with V_{OC} of 0.9V, J_{SC} of 22.94 mA cm^{-2} . When using the passivating ligand 2TI, solar cell performance is significantly improved with a mean PCE, V_{OC} and J_{SC} of 16.6%, 1.02V and 24.05 mA cm^{-2} respectively while a slight improvement is seen in case of 4TmI with a mean PCE, V_{OC} and J_{SC} of 15.7%, 0.96V and an unexpectedly high current of 24.6 mA cm^{-2} respectively.

Annealing of the passivation layers affects device parameters. For 2TI passivated devices, we observe improvements in both PCE and V_{OC} , a trend in contrast with previous works in literature, which report no obvious changes in efficiencies compared to reference[114]. We also observe drops in performance characteristics on increasing the annealing time for 4TmI passivated devices, which can be ascribed to increasing energy misalignment resulting in high interface recombination observed in XEOL and consequently, V_{OC} .

Contrary to the results obtained from XBIC measurements, 2TI devices show slightly lower J_{SC} compared to 4TmI devices. This deviation can presumably arise from the variation in photons flux and energy incident on the active layer in the two techniques, leading to variations in injection dynamics and recombination at the interface. From previous work, 2T molecules have been reported to require excitation wavelength greater than 400nm due to their large bandgap ($>3\text{eV}$)[93]. This essentially means that 2TI 2D layer absorbs only part of the solar spectrum in our J-V measurements but would show greater affinity for X Ray photon absorption, likely leading to secondary carriers and multiplying the generated carrier density in the material[115]. This is reflected in the amplified current intensity obtained in XBIC maps. It is also to be noted that the localized carrier extraction measured for a sample area of $24 \times 24 \mu\text{m}^2$ in XBIC may not translate

proportionally to a much larger active perovskite area in our device (2.5 cm x2.5 cm), due to non-uniformity in ligand deposition affecting hole extraction to HTL.

Overall, the champion device was obtained by annealing the 2TI surface treatment layer for 10 min, with a PCE of 20.13%, a V_{OC} of 1.07 V, a J_{SC} of 24.79 mA cm⁻², and a fill factor (FF) of 78.29% (Table S1, SI). A stabilized PCE of 19.51% is obtained on maximum power point tracking. In contrast, the best performing device with 4TmI treatment gave a PCE of 19.87% after annealing for 10 min, V_{OC} of 1.06 V, J_{SC} of 25.67 mA cm⁻², a fill factor (FF) of 81.24% and a stabilized PCE of 18.12% under MPP tracking.

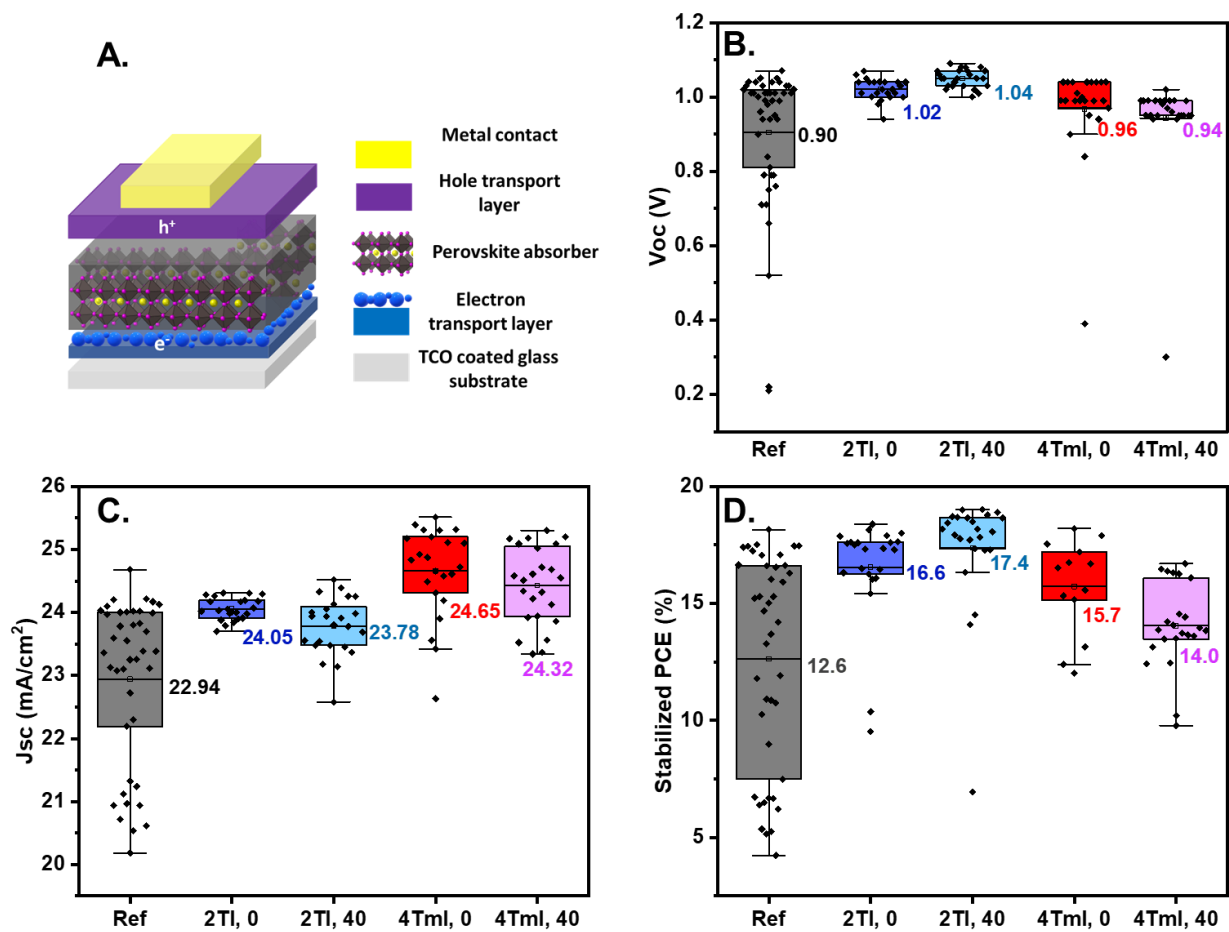


Figure 5.3 Statistics of device performance for perovskite solar cells with different passivation layers (a) device schematic, (b) V_{oc} , (c) J_{sc} , and (d) PCE (mean PCE is shown beside the boxes). Device parameters are obtained from reverse J–V scans.

Table 2. Summary of photovoltaic performance of reference and 2TI/4TmI passivated devices

Variable	Champion PCE (%)	Median PCE (%)	Mean PCE (%)	V _{oc} (V)	J _{sc} (mA/cm ²)	FF (%)	Stabilized MPP (%)
Reference	19.17	14.76	12.6	1.07	24.68	77.57	18.15
2TI, 0	19.03	18.41	16.6	1.07	24.31	79.76	18.38
2TI, 10	20.13	19.03	17.1	1.07	24.79	78.29	19.51
2TI, 40	19.60	18.82	17.4	1.09	24.52	78.35	19.01
4TmI, 0	19.40	16.63	15.7	1.04	25.51	76.40	18.20
4TmI, 10	19.87	16.13	13.6	1.06	25.67	81.24	18.12
4TmI, 40	16.80	14.88	14.0	1.02	25.30	67.38	16.70

5.3 Mechanism and Conclusion

Solar cell performances can be compromised by phase conversion issues at PSC interfaces, particularly when transitioning from cubic perovskite to lower dimensional phases. This transition is often associated with long chain ligands consisting of organic terminal groups, that anchor onto the perovskite surface and form a spacer layer. In the case of CsFA-2TI, the investigations presented in this thesis confirmed compositional changes at the interface and the existence of a 2D Ruddlesden-Popper phase within the first 10 min of annealing. To assess the impact of heat induced changes on charge transport, synchrotron-based XBIC measurements were conducted, revealing significantly enhanced charge extraction in CsFA-2TI devices compared to CsFA control devices. To understand the origin of observed device improvements with bulky cation additives, two major questions are addressed - (i) the reason for higher current in 2TI despite the 2D phase change, and (ii) the correlation between localized carrier transport dynamics and device performances.

To the first question- in lower dimensional perovskites with multiple quantum wells, charges tend to localize at the organic spacer layer which hinders their transport and subsequent current flow. However, depending on the nature of the chosen interlayer cation, the electronic and dielectric confinement effects in these structures can be tuned[20]. Specifically, cations containing electron-rich conjugated rings are deemed as more polarizable, mitigating the charge confinement typical in these systems. Several hybrid, layered perovskites based on thiophene alkylammonium cations with one, two, or four, thiophene units have been reported[116-119].

The influence of cation modification on the surface energy landscape was studied using KPFM measurements. Results suggest that work function changes induced by 2TI and 4TmI passivation alter the nature of surface termination and the extent of band bending. Under illumination, the initially upward bent bands at the passivation/HTL interface become flatter, lowering the potential barrier. This effect is evidently more pronounced for 2TI than for 4TmI, as seen from the magnitudes of SPV, further suggesting that CsFA-2TI lowered the barrier for hole extraction at the interface compared to untreated reference film, while the CsFA-4TmI system did not significantly contribute to hole extraction, aligning with the lower current seen in XBIC. To further understand the deviation of 2TI behavior from 4TmI, DFT results reveal that $2T^+$ cations are weakly bound to the surface compared to $4Tm^+$. Coupled with the fact that $2T^+$ vacancies are likely created during high- temperature annealing over an extended period, the short diffusion distance of holes from perovskite to HTL facilitates charge transfer, surpassing the barrier.

Addressing the second question involves considering the caveats that lead to differences between micro-scale currents seen in XBIC and in-house J-V measurements. Despite limitations such as the different optical response in 2TI due to its large bandgap, larger illumination area in the fabricated devices and cation coverage heterogeneity, the effect of defect passivation is evident

in the higher overall performances in 2TI and 4TmI devices. As expected, the behavior of 4TmI layer differs from 2TI due to its greater bulkiness and limited spatial mobility. Although the 4TmI interface transitions to RP phase over longer timescale, highlighting the stability of this surface treatment layer, the final CsFA-4TmI devices show poor hole extraction and low open circuit voltages as well as fill factor. These results highlight the dichotomy between capping layer stability and layer conductivity because of varying steric sizes, where bulkier cations with restricted spatial mobility promote layer stabilization but simultaneously introduce a thicker barrier layer impeding hole transport.

CHAPTER 6. CONCLUSIONS AND OUTLOOK

6.1 Summary

This thesis aims to achieve heat-stable perovskite solar cells employing the surface treatment strategy. We have explored the role that bulky conjugated ligands 2TI and 4TmI play in determining heat induced structural changes at perovskite/HTL interfaces and their effects on solar cell characteristics.

In chapter 4, the 2TI and 4TmI ligands used to passivate the perovskite surface show phase transition to lower dimensional phases under thermal stress. However, changing the length of the spacer cation gives the opportunity to tune the stability of interfacial perovskite structure. Evident from GIWAXS, 2TI- on account of its smaller size and greater mobility, results in faster phase reconstruction in 2TI passivation layer versus the larger sized 4TmI. XPS further sheds light on the size dependent thermal diffusion behavior of the two ligands. With prolonged heating, 2TI cations tend to disappear from the surface while 4TmI cations tend to localize, breaking apart the strong inter-molecular forces and homogenizing on the surface.

Despite phase changes, 2TI treated devices can extract holes efficiently, tune the surface potential to promote hole extraction and reduces recombination at perovskite/hole transport layer interface. Chapter 5 discusses these superior properties which result in increased 2TI/CsFA based solar cell efficiency of 20.13%. At the same time, the obtained improvements can be countered by a too thick passivation layer consisting of larger sized 4TmI that is strongly bonded to the perovskite surface, forming an organic barrier under prolonged heating. This impedes carrier extraction, manifesting in higher recombination, lower V_{OC} and low PCEs under thermal exposure. In both the cases with 2TI and 4TmI surface treatment, KPFM results suggest that films without

passivation show a substantially varying surface potential, whereas films with passivation layer help preserve the initial potential response on annealing. These observations suggest that, by optimizing the length of cation backbone and cation-perovskite interactions, it is possible to achieve both stability and enhanced carrier extraction at passivated surfaces.

6.2 Future Work

This dissertation seeks to determine the impact of size dependent diffusion behavior of organic ligands on phase perturbation and device characteristics, with the aim that performances remain unaltered at high operating temperatures. Chapters 4 and 5 address the challenge of thermal instabilities in perovskite structure and their effect on PSC performances. However, PSCs also show considerable degradation under light possibly due to ion migration. The passivation of surface defect sites- which function as primary ion migration channels- can help mitigate the photo-induced degradation[69]. Formation of low dimensional perovskites is also excellent in suppressing the migration mobility of halide ions by protecting the perovskite film surface[120]. Thus, surface passivation using bulky cations can show multi-faceted effects on ion migration- by curbing the formation of defects, and forming the 2D observed in my studies, both of which will prevent ion migration related hysteresis in the long term[121]. Thus, it would be interesting from both a scientific and practical standpoint to study the effects of bulky cation passivation layer on stability under illumination and further increase cation functionalities.

Further, chapter 5 discusses device results highlighting the role of conjugated organic ligands on the electronic properties of heterointerfaces. This correlation warrants further investigation, as it can open avenues for the use of 2D capping layer in applications such as lasers and diodes. As an example, amine-based passivation agents have been used with MAPbI₃ to develop light emitting diodes with enhanced photoluminescence and long-term stability[122]. This

makes organic 2TI- which can reduce non-radiative recombination and enhances charge extraction, an interesting option to explore.

Additionally, in chapter 5, using bulky cation additives is shown to be beneficial in enhancing device PCEs and minimizing current loss under thermal stress when employed in direct n-i-p device configuration. By identifying the potential of conjugated organic molecules in tailoring interface structures, this work provides guidelines for selection and design of suitable passivation materials. This understanding can be applied beyond the current work and can be particularly useful for inverted p-i-n devices which suffer from low PCEs. Quaternary- and di-ammonium ligands with multiple $-\text{NH}_3^+$ groups have been reported to regulate surface potential and introduce passivation effects for V_{OC} and PCE improvements in these device configurations[123-125]. This introduces the possibility of employing 2TI and 4TmI in a similar capacity, resulting in long-term performance gains.

APPENDIX. SUPPORTING INFORMATION

Perovskite film fabrication

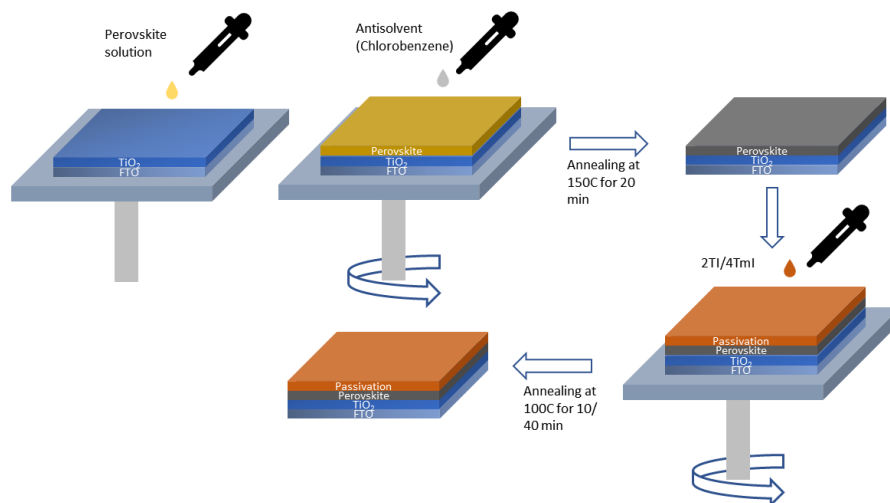


Figure A1. Spin coating method used to deposit perovskite and passivation layers. 4mM solutions of 2TI (1.35mg/mL) and 4TmI (2.12mg/mL) dissolved in isopropyl alcohol were spin coated on CsFAPbI₃ thin films.

Film Morphology

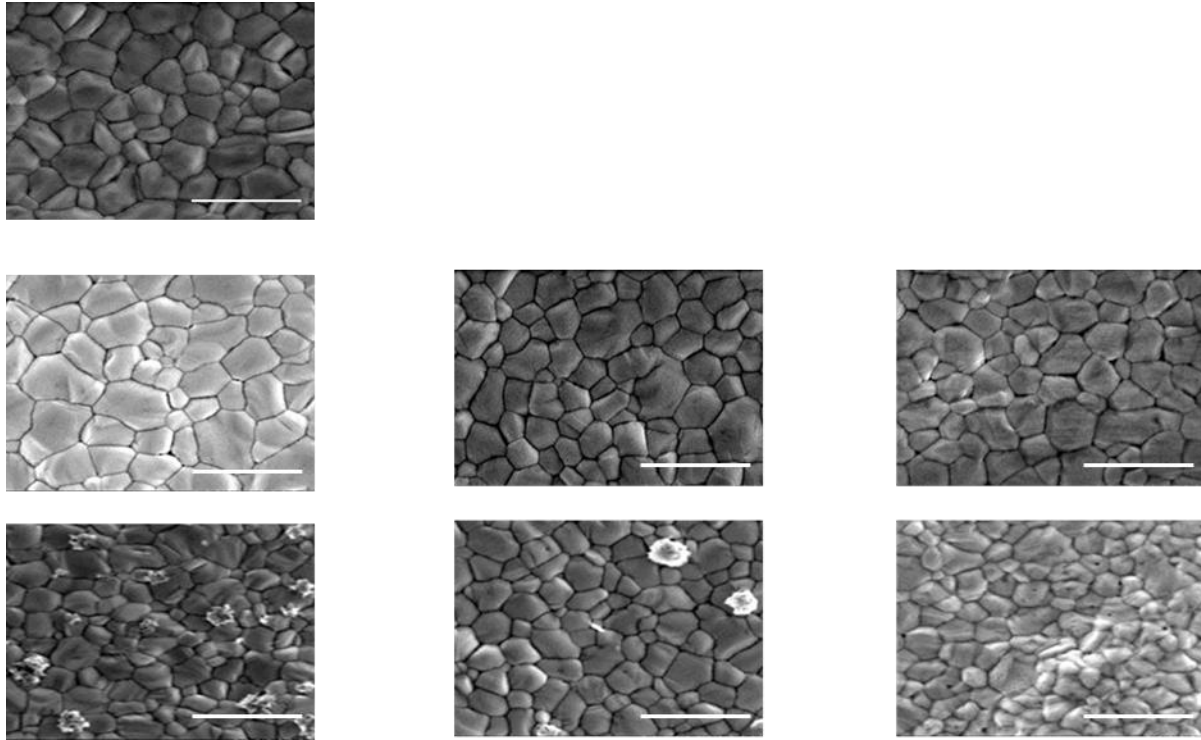


Figure A2. Surface morphology of the perovskite films treated with Ref, 2TI and 4TmI (top to bottom) after 0, 10 and 40 minutes annealing (left to right). Scale bar is 1 μ m.

Surface Composition Analysis

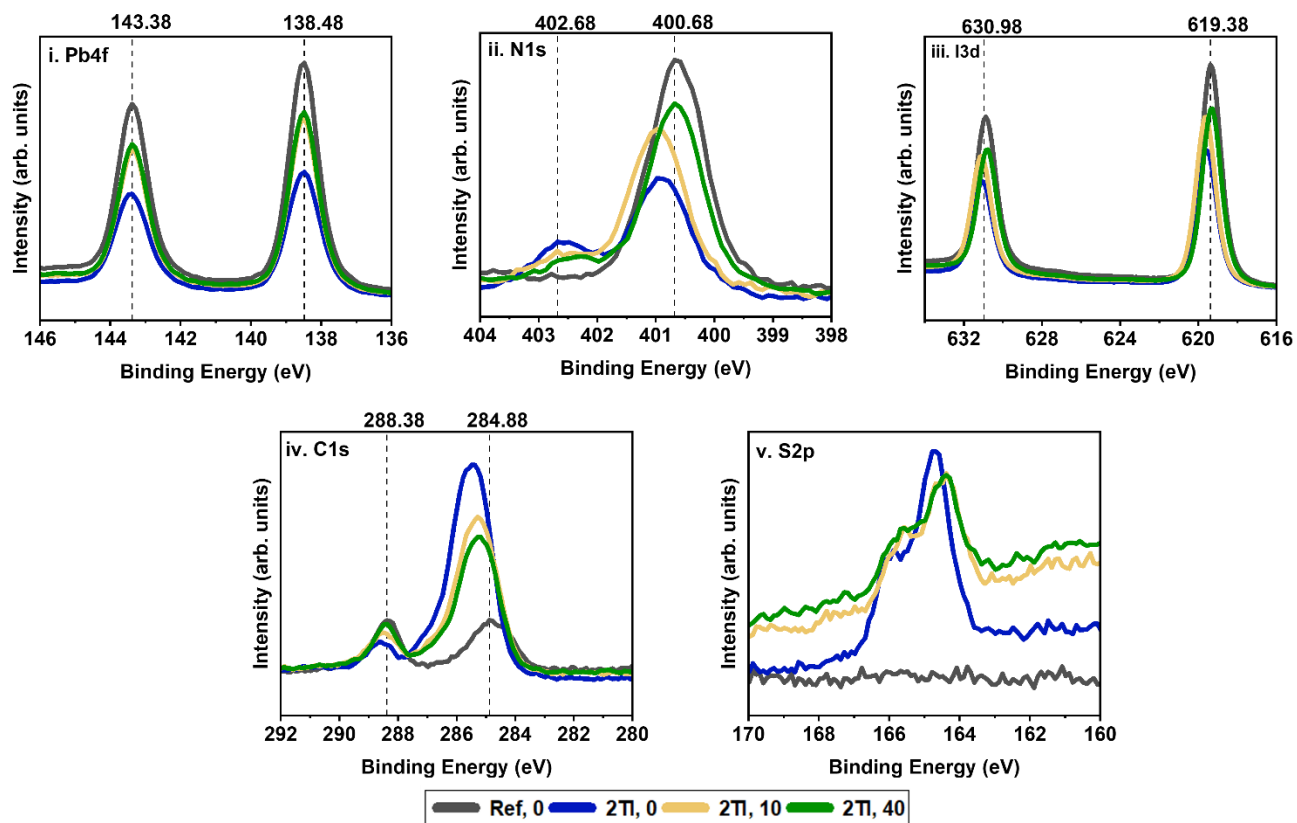


Figure A3. XPS elemental scans for Pb 4f, N 1s, I 3d, C 1s and S 2p on the top surface of perovskite films treated with 2TI molecules.

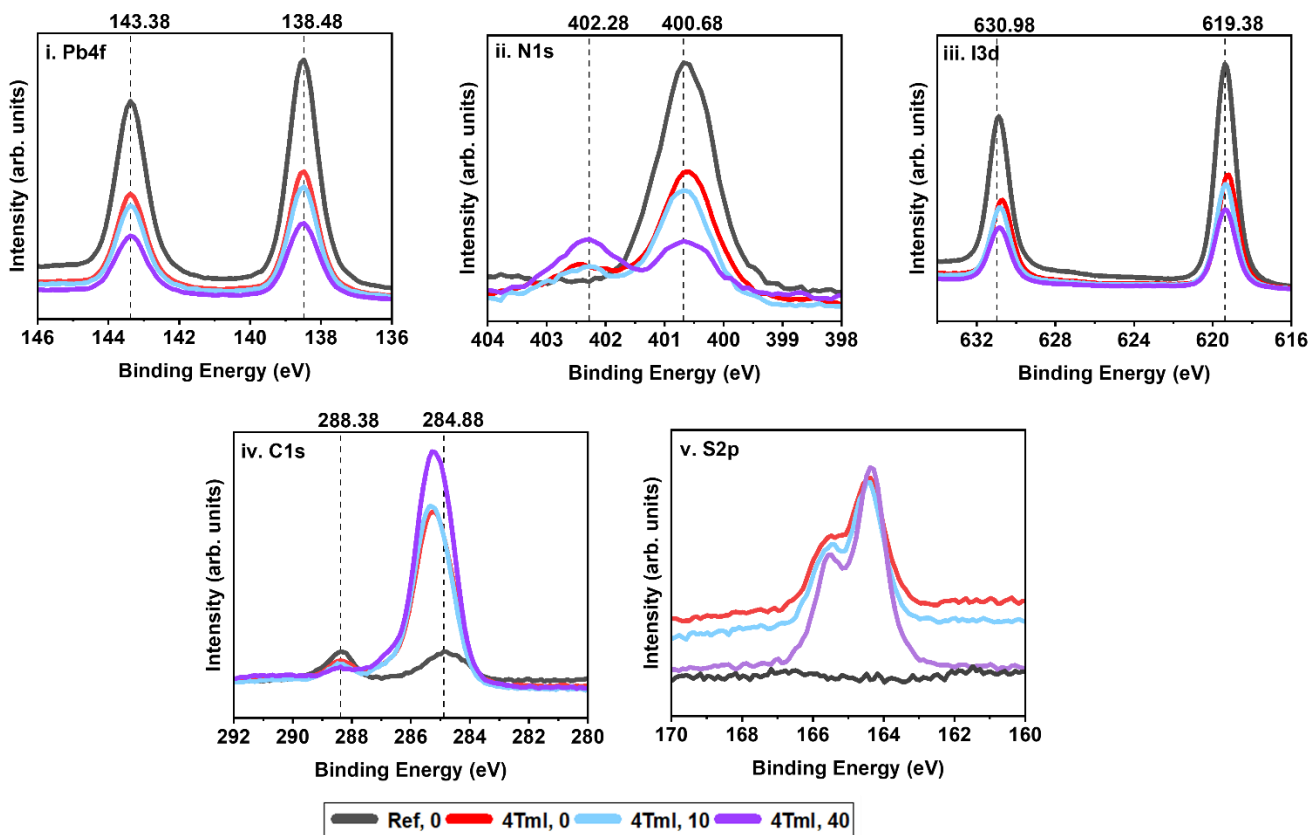


Figure A4. XPS elemental scans for Pb 4f, N 1s, I 3d, C 1s and S 2p on the top surface of perovskite films treated with 4TmI molecules.

Surface Structure Analysis

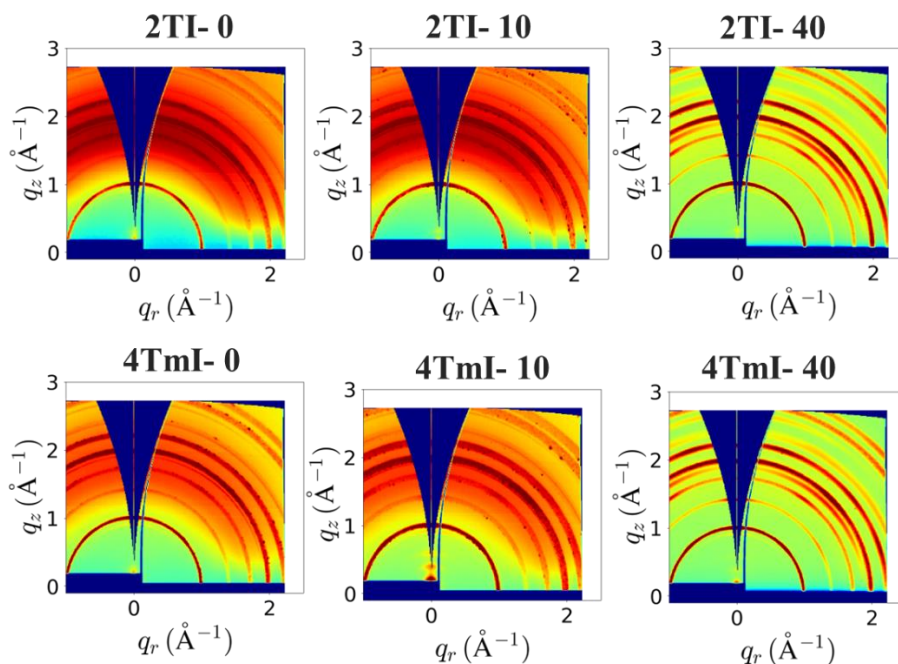


Figure A5. GIWAXS profiles show changes in crystal structure of the interfaces treated with 2TI and 4TmI (top to bottom) after 0-, 10- and 40-minutes annealing (left to right).

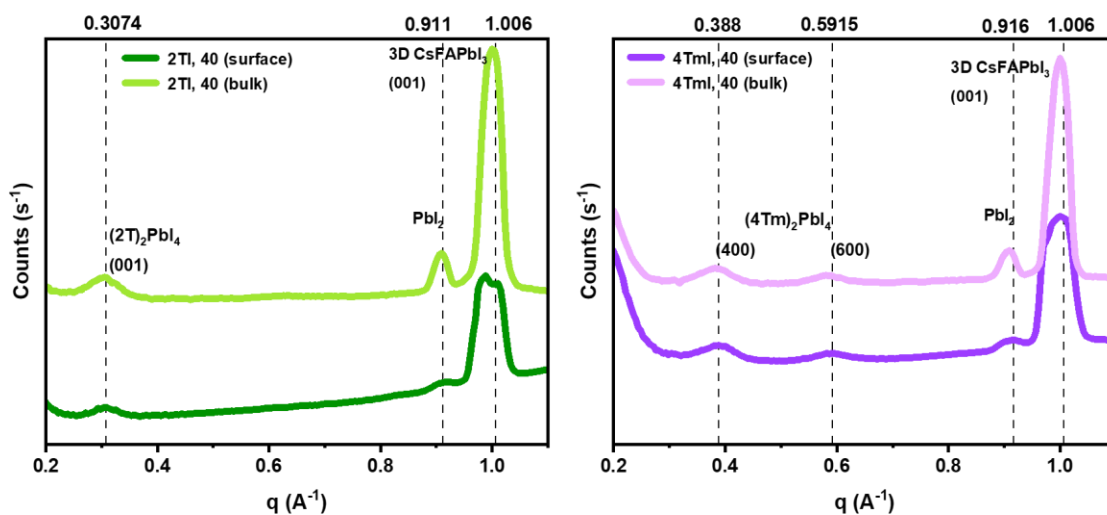


Figure A6. Comparison of surface versus bulk crystallinity of 2D $(2T)_2PbI_4$ and $(4Tm)_2PbI_4$ layers after 40 min anneal.

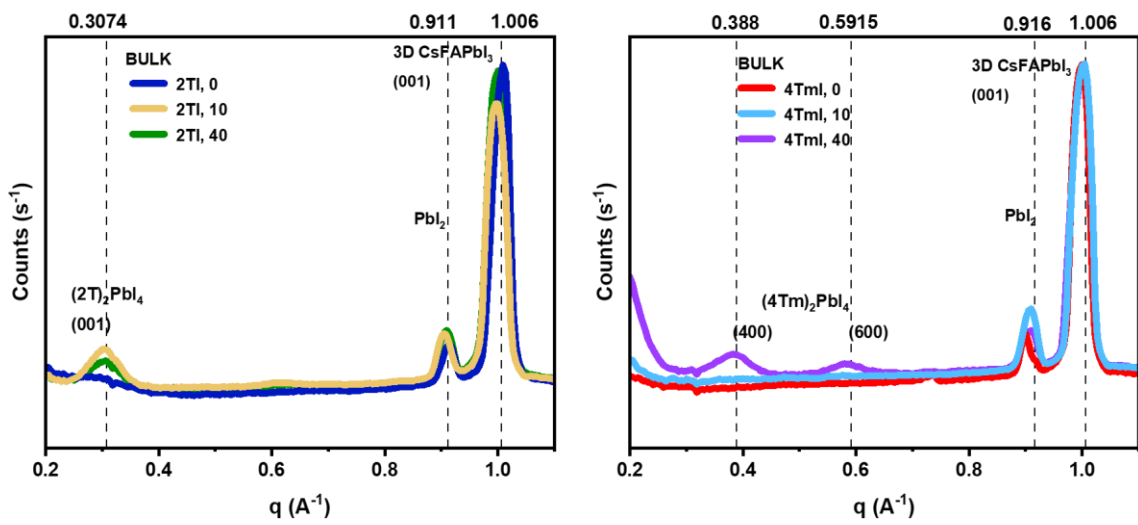


Figure A7. Evolution of the 2TI and 4TmI layer in bulk with annealing.

KPFM Surface potential distribution

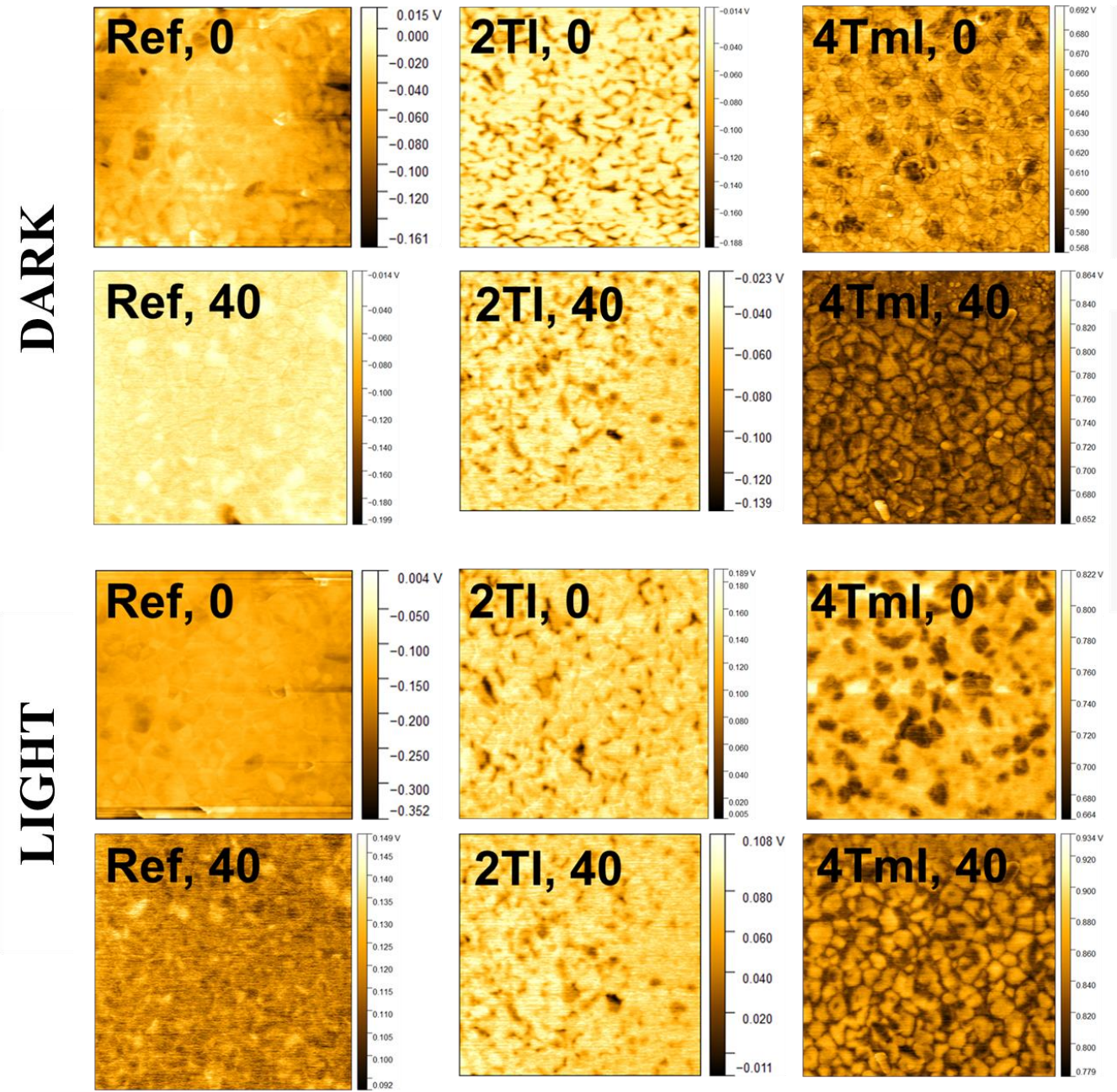


Figure A8. Spatial maps showing Contact Potential Distributions in dark and light.

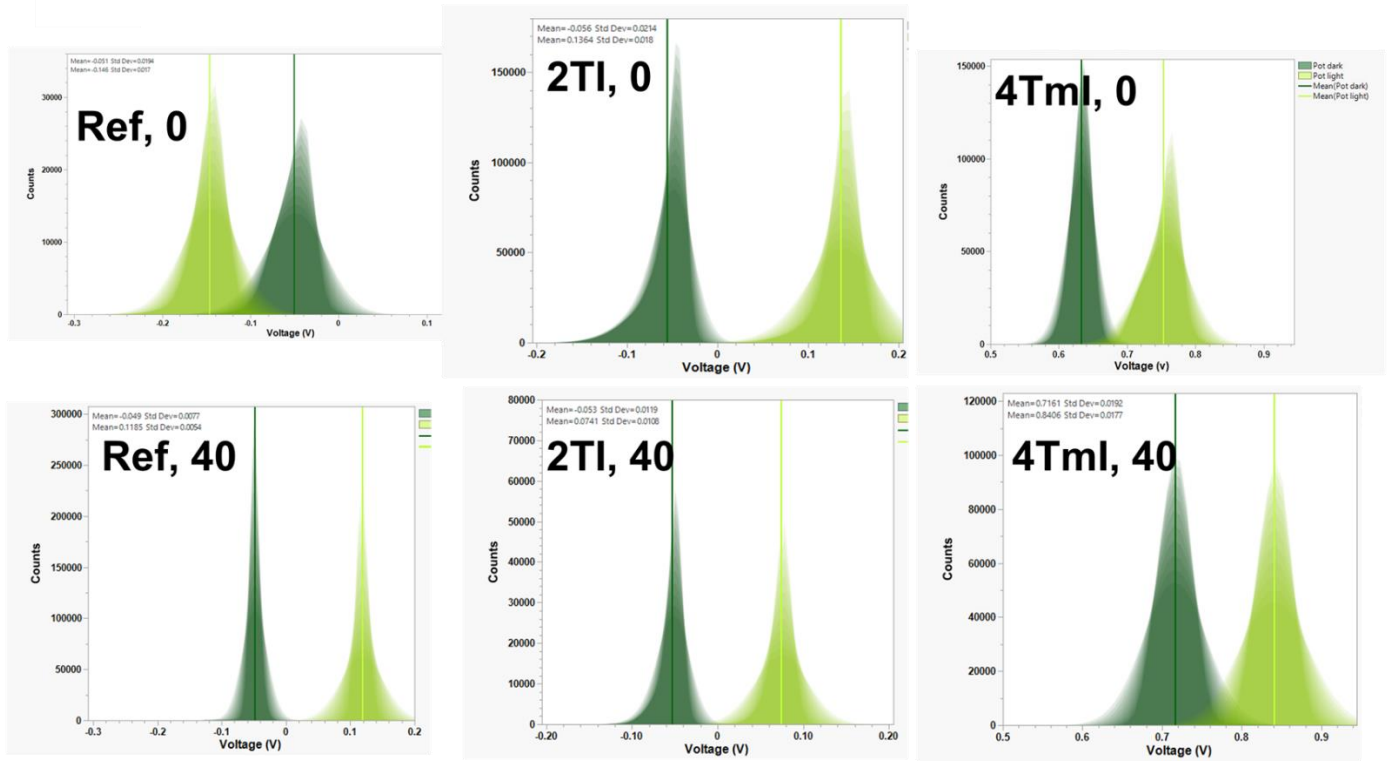


Figure A9. Contact Potential Distributions showing potential spread and mean used for SPV ($CPD_{mean}(light) - CPD_{mean}(dark)$).

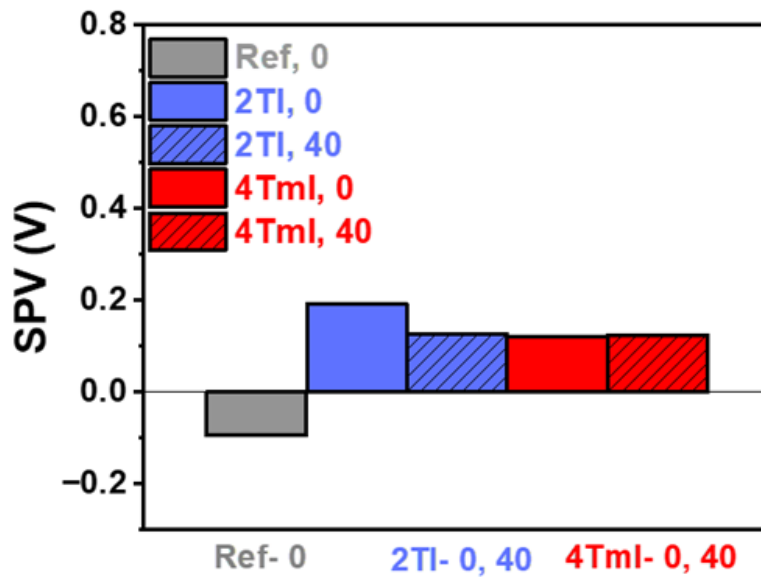


Figure A10. Surface Photovoltage histogram.

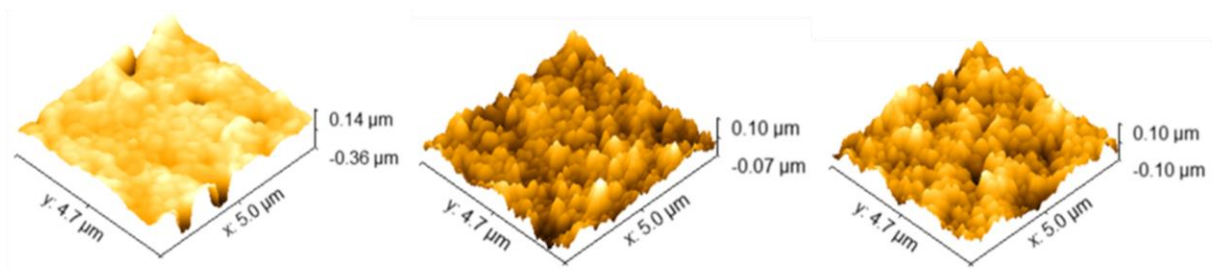


Figure A11. Topography of reference versus passivated perovskite.

REFERENCES

- [1] R. e. i. d. a. c. f.-e. OECD (2023).
- [2] F. Creutzig, P. Agoston, J. C. Goldschmidt, G. Luderer, G. Nemet, and R. C. Pietzcker, "The underestimated potential of solar energy to mitigate climate change," *Nature Energy*, vol. 2, no. 9, pp. 1-9, 2017.
- [3] M. M. Rahman *et al.*, "End-of-Life Photovoltaic Recycled Silicon: A Sustainable Circular Materials Source for Electronic Industries," *Advanced Energy and Sustainability Research*, vol. 2, 05/05 2021, doi: 10.1002/aesr.202100081.
- [4] N. R. E. Laboratory. Interactive Best Research-Cell Efficiency Chart
- [5] E. C. BELLINI, "EPFL achieve 31.25% efficiency for tandem perovskite-silicon solar cell, 2022)."
- [6] Y. Liu *et al.*, "High-Efficiency Silicon Heterojunction Solar Cells: Materials, Devices and Applications," *Materials Science and Engineering: R: Reports*, vol. 142, p. 100579, 2020/10/01/ 2020, doi: <https://doi.org/10.1016/j.mser.2020.100579>.
- [7] S. Almosni *et al.*, "Material challenges for solar cells in the twenty-first century: directions in emerging technologies," (in eng), *Sci Technol Adv Mater*, vol. 19, no. 1, pp. 336-369, 2018, doi: 10.1080/14686996.2018.1433439.
- [8] P. Sharma and P. Goyal, "Evolution of PV technology from conventional to nano-materials," *Materials Today: Proceedings*, vol. 28, pp. 1593-1597, 2020.
- [9] J. Jean, P. R. Brown, R. L. Jaffe, T. Buonassisi, and V. Bulović, "Pathways for solar photovoltaics," *Energy & Environmental Science*, 10.1039/C4EE04073B vol. 8, no. 4, pp. 1200-1219, 2015, doi: 10.1039/C4EE04073B.
- [10] M. A. Green, Y. Hishikawa, E. D. Dunlop, D. H. Levi, J. Hohl-Ebinger, and A. W. Y. Ho-Baillie, "Solar cell efficiency tables (version 52)," *Progress in Photovoltaics: Research and Applications*, vol. 26, no. 7, pp. 427-436, 2018, doi: <https://doi.org/10.1002/pip.3040>.
- [11] F. Iftikhar *et al.*, "Structural and optoelectronic properties of hybrid halide perovskites for solar cells," *Organic Electronics*, vol. 91, p. 106077, 02/01 2021, doi: 10.1016/j.orgel.2021.106077.
- [12] F. Huang, M. Li, P. Siffalovic, G. Cao, and J. Tian, "From scalable solution fabrication of perovskite films towards commercialization of solar cells," *Energy & Environmental Science*, 10.1039/C8EE03025A vol. 12, no. 2, pp. 518-549, 2019, doi: 10.1039/C8EE03025A.
- [13] I. du Fossé *et al.*, "Limits of Defect Tolerance in Perovskite Nanocrystals: Effect of Local Electrostatic Potential on Trap States," *Journal of the American Chemical Society*, vol. 144, no. 25, pp. 11059-11063, 2022/06/29 2022, doi: 10.1021/jacs.2c02027.
- [14] L. Qiu *et al.*, "Engineering Interface Structure to Improve Efficiency and Stability of Organometal Halide Perovskite Solar Cells," *The Journal of Physical Chemistry B*, vol. 122, no. 2, pp. 511-520, 2018/01/18 2018, doi: 10.1021/acs.jpcc.7b03921.

- [15] Q. Zhang *et al.*, "Polymer interface engineering enabling high-performance perovskite solar cells with improved fill factors of over 82%," *Journal of Materials Chemistry C*, 10.1039/C9TC06578D vol. 8, no. 16, pp. 5467-5475, 2020, doi: 10.1039/C9TC06578D.
- [16] S. Lee, S. Hong, H. Lee, and H. Kim, "Perovskite Solar Cells: Interface Engineering of Perovskite/Hole Transport Layer Using Nano-Network Formation in Small Molecule–Polymer Blend for Efficient Inverted Perovskite Solar Cells (Adv. Mater. Interfaces 6/2021)," *Advanced Materials Interfaces*, vol. 8, p. 2170032, 03/01 2021, doi: 10.1002/admi.202170032.
- [17] D. Zhang, D. Li, Y. Hu, A. Mei, and H. Han, "Degradation pathways in perovskite solar cells and how to meet international standards," *Communications Materials*, vol. 3, no. 1, p. 58, 2022/08/29 2022, doi: 10.1038/s43246-022-00281-z.
- [18] J. Song *et al.*, "Thermal instability originating from the interface between organic–inorganic hybrid perovskites and oxide electron transport layers," *Energy & Environmental Science*, 10.1039/D2EE02649J vol. 15, no. 11, pp. 4836-4849, 2022, doi: 10.1039/D2EE02649J.
- [19] A. A. Sutanto *et al.*, "Dynamical evolution of the 2D/3D interface: a hidden driver behind perovskite solar cell instability," *Journal of Materials Chemistry A*, 10.1039/C9TA12489F vol. 8, no. 5, pp. 2343-2348, 2020, doi: 10.1039/C9TA12489F.
- [20] E. Mahal, S. C. Mandal, and B. Pathak, "Understanding the role of spacer cation in 2D layered halide perovskites to achieve stable perovskite solar cells," *Materials Advances*, 10.1039/D1MA01135A vol. 3, no. 5, pp. 2464-2474, 2022, doi: 10.1039/D1MA01135A.
- [21] E. Katz, "Perovskite: Name Puzzle and German-Russian Odyssey of Discovery," *Helvetica Chimica Acta*, vol. 103, 04/16 2020, doi: 10.1002/hlca.202000061.
- [22] Y.-T. Huang, S. R. Kavanagh, D. O. Scanlon, A. Walsh, and R. L. Hoyer, "Perovskite-inspired materials for photovoltaics and beyond—from design to devices," *Nanotechnology*, vol. 32, no. 13, p. 132004, 2021.
- [23] H. L. Wells, "Über die cäsium-und kalium-bleihalogenide," *Zeitschrift für anorganische Chemie*, vol. 3, no. 1, pp. 195-210, 1893.
- [24] Y. Sun *et al.*, "Bright and stable perovskite light-emitting diodes in the near-infrared range," *Nature*, vol. 615, no. 7954, pp. 830-835, 2023/03/01 2023, doi: 10.1038/s41586-023-05792-4.
- [25] A. K. Jena, A. Kulkarni, and T. Miyasaka, "Halide Perovskite Photovoltaics: Background, Status, and Future Prospects," *Chemical Reviews*, vol. 119, no. 5, pp. 3036-3103, 2019/03/13 2019, doi: 10.1021/acs.chemrev.8b00539.
- [26] Y. Tang *et al.*, "Enabling low-drift flexible perovskite photodetectors by electrical modulation for wearable health monitoring and weak light imaging," *Nature Communications*, vol. 14, no. 1, p. 4961, 2023/08/16 2023, doi: 10.1038/s41467-023-40711-1.
- [27] Q. Zhang, Q. Shang, R. Su, T. T. H. Do, and Q. Xiong, "Halide Perovskite Semiconductor Lasers: Materials, Cavity Design, and Low Threshold," *Nano Letters*, vol. 21, no. 5, pp. 1903-1914, 2021/03/10 2021, doi: 10.1021/acs.nanolett.0c03593.

- [28] J. S. Manser, J. A. Christians, and P. V. Kamat, "Intriguing Optoelectronic Properties of Metal Halide Perovskites," *Chemical Reviews*, vol. 116, no. 21, pp. 12956-13008, 2016/11/09 2016, doi: 10.1021/acs.chemrev.6b00136.
- [29] S. Colella *et al.*, "MAPbI₃-xCl_x Mixed Halide Perovskite for Hybrid Solar Cells: The Role of Chloride as Dopant on the Transport and Structural Properties," *Chemistry of Materials*, vol. 25, pp. 4613–4618, 11/11 2013, doi: 10.1021/cm402919x.
- [30] J. Navas *et al.*, "New insights into organic–inorganic hybrid perovskite CH₃NH₃PbI₃ nanoparticles. An experimental and theoretical study of doping in Pb²⁺ sites with Sn²⁺, Sr²⁺, Cd²⁺ and Ca²⁺," *Nanoscale*, 10.1039/C5NR00041F vol. 7, no. 14, pp. 6216-6229, 2015, doi: 10.1039/C5NR00041F.
- [31] G.-W. Kim and A. Petrozza, "Defect Tolerance and Intolerance in Metal-Halide Perovskites," *Advanced Energy Materials*, vol. 10, no. 37, p. 2001959, 2020, doi: <https://doi.org/10.1002/aenm.202001959>.
- [32] R. E. Brandt *et al.*, "Searching for “defect-tolerant” photovoltaic materials: combined theoretical and experimental screening," *Chemistry of Materials*, vol. 29, no. 11, pp. 4667-4674, 2017.
- [33] R. C. Kurchin, P. Gorai, T. Buonassisi, and V. Stevanović, "Structural and Chemical Features Giving Rise to Defect Tolerance of Binary Semiconductors," *Chemistry of Materials*, vol. 30, no. 16, pp. 5583-5592, 2018/08/28 2018, doi: 10.1021/acs.chemmater.8b01505.
- [34] T. He *et al.*, "Reduced-dimensional perovskite photovoltaics with homogeneous energy landscape," *Nature Communications*, vol. 11, no. 1, p. 1672, 2020/04/03 2020, doi: 10.1038/s41467-020-15451-1.
- [35] J. Qiu, Y. Zheng, Y. Xia, L. Chao, Y. Chen, and W. Huang, "Rapid Crystallization for Efficient 2D Ruddlesden–Popper (2DRP) Perovskite Solar Cells," *Advanced Functional Materials*, vol. 29, no. 47, p. 1806831, 2019, doi: <https://doi.org/10.1002/adfm.201806831>.
- [36] C. Fu *et al.*, "From Structural Design to Functional Construction: Amine Molecules in High-Performance Formamidinium-Based Perovskite Solar Cells," *Angewandte Chemie International Edition*, vol. 61, no. 19, p. e202117067, 2022, doi: <https://doi.org/10.1002/anie.202117067>.
- [37] X. Li *et al.*, "Two-Dimensional Dion–Jacobson Hybrid Lead Iodide Perovskites with Aromatic Diammonium Cations," *Journal of the American Chemical Society*, vol. 141, no. 32, pp. 12880-12890, 2019/08/14 2019, doi: 10.1021/jacs.9b06398.
- [38] C. M. M. Soe *et al.*, "New Type of 2D Perovskites with Alternating Cations in the Interlayer Space, (C(NH₂)₃)(CH₃NH₃)_nPb_nI_{3n+1}: Structure, Properties, and Photovoltaic Performance," *Journal of the American Chemical Society*, vol. 139, no. 45, pp. 16297-16309, 2017/11/15 2017, doi: 10.1021/jacs.7b09096.
- [39] R. Younts *et al.*, "Efficient generation of long-lived triplet excitons in 2D hybrid perovskite," *Advanced materials (Deerfield Beach, Fla.)*, vol. 29, no. 9, 2017.

- [40] K.-z. Du *et al.*, "Two-dimensional lead (II) halide-based hybrid perovskites templated by acene alkylamines: crystal structures, optical properties, and piezoelectricity," *Inorganic chemistry*, vol. 56, no. 15, pp. 9291-9302, 2017.
- [41] Y. Miao, Y. Chen, H. Chen, X. Wang, and Y. Zhao, "Using steric hindrance to manipulate and stabilize metal halide perovskites for optoelectronics," *Chemical Science*, 10.1039/D1SC01171E vol. 12, no. 21, pp. 7231-7247, 2021, doi: 10.1039/D1SC01171E.
- [42] G. Grancini *et al.*, "One-Year stable perovskite solar cells by 2D/3D interface engineering," *Nature communications*, vol. 8, no. 1, p. 15684, 2017.
- [43] C. Ma *et al.*, "2D/3D perovskite hybrids as moisture-tolerant and efficient light absorbers for solar cells," *Nanoscale*, Article vol. 8, no. 43, pp. 18309-18314, 2016, doi: 10.1039/c6nr04741f.
- [44] W. Xiang, J. Zhang, S. Liu, S. Albrecht, A. Hagfeldt, and Z. Wang, "Intermediate phase engineering of halide perovskites for photovoltaics," *Joule*, vol. 6, no. 2, pp. 315-339, 2022/02/16/ 2022, doi: <https://doi.org/10.1016/j.joule.2021.11.013>.
- [45] A. T. Mallajosyula *et al.*, "Large-area hysteresis-free perovskite solar cells via temperature controlled doctor blading under ambient environment," *Applied Materials Today*, vol. 3, pp. 96-102, 2016/06/01/ 2016, doi: <https://doi.org/10.1016/j.apmt.2016.03.002>.
- [46] F. C. Krebs, "Fabrication and processing of polymer solar cells: A review of printing and coating techniques," *Solar Energy Materials and Solar Cells*, vol. 93, no. 4, pp. 394-412, 2009/04/01/ 2009, doi: <https://doi.org/10.1016/j.solmat.2008.10.004>.
- [47] T. I. Alanazi, "Current spray-coating approaches to manufacture perovskite solar cells," *Results in Physics*, vol. 44, p. 106144, 2023/01/01/ 2023, doi: <https://doi.org/10.1016/j.rinp.2022.106144>.
- [48] L.-H. Chou, J. M. W. Chan, and C.-L. Liu, "Progress in Spray Coated Perovskite Films for Solar Cell Applications," *Solar RRL*, vol. 6, no. 4, p. 2101035, 2022, doi: <https://doi.org/10.1002/solr.202101035>.
- [49] Y. Zheng *et al.*, "Spray coating of the PCBM electron transport layer significantly improves the efficiency of p-i-n planar perovskite solar cells," *Nanoscale*, 10.1039/C8NR01763H vol. 10, no. 24, pp. 11342-11348, 2018, doi: 10.1039/C8NR01763H.
- [50] L.-H. Chou, Y.-T. Yu, I. Osaka, X.-F. Wang, and C.-L. Liu, "Spray deposition of NiOx hole transport layer and perovskite photoabsorber in fabrication of photovoltaic mini-module," *Journal of Power Sources*, vol. 491, p. 229586, 2021/04/15/ 2021, doi: <https://doi.org/10.1016/j.jpowsour.2021.229586>.
- [51] K. Han *et al.*, "Fully solution processed semi-transparent perovskite solar cells with spray-coated silver nanowires/ZnO composite top electrode," *Solar Energy Materials and Solar Cells*, vol. 185, pp. 399-405, 2018/10/01/ 2018, doi: <https://doi.org/10.1016/j.solmat.2018.05.048>.
- [52] J.-H. Lee, B. S. Kim, J. Park, J.-W. Lee, and K. Kim, "Opportunities and Challenges for Perovskite Solar Cells Based on Vacuum Thermal Evaporation," *Advanced Materials*

- Technologies*, vol. 8, no. 20, p. 2200928, 2023, doi: <https://doi.org/10.1002/admt.202200928>.
- [53] F. U. Kosasih, E. Erdenebileg, N. Mathews, S. G. Mhaisalkar, and A. Bruno, "Thermal evaporation and hybrid deposition of perovskite solar cells and mini-modules," *Joule*, vol. 6, no. 12, pp. 2692-2734, 2022/12/21/ 2022, doi: <https://doi.org/10.1016/j.joule.2022.11.004>.
- [54] Q. C. Burlingame, A. B. Kaplan, T. Liu, and Y.-L. Loo, "Persistent iodine contamination resulting from thermal evaporation of inorganic perovskites," *Journal of Vacuum Science & Technology B*, vol. 40, no. 6, 2022, doi: 10.1116/6.0002174.
- [55] R. Checharoen *et al.*, "Encapsulating perovskite solar cells to withstand damp heat and thermal cycling," *Sustainable Energy & Fuels*, 10.1039/C8SE00250A vol. 2, no. 11, pp. 2398-2406, 2018, doi: 10.1039/C8SE00250A.
- [56] K. A. Bush *et al.*, "23.6%-efficient monolithic perovskite/silicon tandem solar cells with improved stability," *Nature Energy*, vol. 2, no. 4, p. 17009, 2017/02/17 2017, doi: 10.1038/nenergy.2017.9.
- [57] X. Zhang *et al.*, "Rapid degradation behavior of encapsulated perovskite solar cells under light, bias voltage or heat fields," (in eng), *Nanoscale Adv*, vol. 3, no. 21, pp. 6128-6137, Oct 27 2021, doi: 10.1039/d1na00495f.
- [58] K. Domanski, E. A. Alharbi, A. Hagfeldt, M. Grätzel, and W. Tress, "Systematic investigation of the impact of operation conditions on the degradation behaviour of perovskite solar cells," *Nature Energy*, vol. 3, no. 1, pp. 61-67, 2018/01/01 2018, doi: 10.1038/s41560-017-0060-5.
- [59] J.-Y. Seo *et al.*, "Novel p-dopant toward highly efficient and stable perovskite solar cells," *Energy & Environmental Science*, vol. 11, no. 10, pp. 2985-2992, 2018.
- [60] I. Deretzis *et al.*, "Exploring the Structural Competition between the Black and the Yellow Phase of CsPbI₃," *Nanomaterials*, vol. 11, no. 5, p. 1282, 2021. [Online]. Available: <https://www.mdpi.com/2079-4991/11/5/1282>.
- [61] L.-Q. Xie *et al.*, "Understanding the Cubic Phase Stabilization and Crystallization Kinetics in Mixed Cations and Halides Perovskite Single Crystals," *Journal of the American Chemical Society*, vol. 139, no. 9, pp. 3320-3323, 2017/03/08 2017, doi: 10.1021/jacs.6b12432.
- [62] D.-H. Choi, H.-J. Seok, S.-K. Kim, D.-H. Kim, B. Hou, and H.-K. Kim, "The Effect of Cs/FA Ratio on the Long-Term Stability of Mixed Cation Perovskite Solar Cells," *Solar RRL*, vol. 5, no. 12, p. 2100660, 2021, doi: <https://doi.org/10.1002/solr.202100660>.
- [63] J.-W. Lee, D.-H. Kim, H.-S. Kim, S.-W. Seo, S. M. Cho, and N.-G. Park, "Formamidinium and Cesium Hybridization for Photo- and Moisture-Stable Perovskite Solar Cell," *Advanced Energy Materials*, vol. 5, no. 20, p. 1501310, 2015, doi: <https://doi.org/10.1002/aenm.201501310>.
- [64] M. Saliba *et al.*, "Cesium-containing triple cation perovskite solar cells: improved stability, reproducibility and high efficiency," *Energy & Environmental Science*, 10.1039/C5EE03874J vol. 9, no. 6, pp. 1989-1997, 2016, doi: 10.1039/C5EE03874J.

- [65] Y. An *et al.*, "Structural Stability of Formamidinium- and Cesium-Based Halide Perovskites," *ACS Energy Letters*, vol. 6, no. 5, pp. 1942-1969, 2021/05/14 2021, doi: 10.1021/acsenergylett.1c00354.
- [66] J. Zhao *et al.*, "Strained hybrid perovskite thin films and their impact on the intrinsic stability of perovskite solar cells," *Science Advances*, vol. 3, no. 11, p. eaao5616, 2017, doi: doi:10.1126/sciadv.aao5616.
- [67] T. J. McMahon, "Accelerated testing and failure of thin-film PV modules," *Progress in Photovoltaics: Research and Applications*, vol. 12, no. 2-3, pp. 235-248, 2004, doi: <https://doi.org/10.1002/pip.526>.
- [68] M. Dailey, Y. Li, and A. D. Printz, "Residual Film Stresses in Perovskite Solar Cells: Origins, Effects, and Mitigation Strategies," (in eng), *ACS Omega*, vol. 6, no. 45, pp. 30214-30223, Nov 16 2021, doi: 10.1021/acsomega.1c04814.
- [69] E. Bi, Z. Song, C. Li, Z. Wu, and Y. Yan, "Mitigating ion migration in perovskite solar cells," *Trends in Chemistry*, vol. 3, no. 7, pp. 575-588, 2021/07/01/ 2021, doi: <https://doi.org/10.1016/j.trechm.2021.04.004>.
- [70] J. Mizusaki, K. Arai, and K. Fueki, "Ionic conduction of the perovskite-type halides," *Solid State Ionics*, vol. 11, no. 3, pp. 203-211, 1983/11/01/ 1983, doi: [https://doi.org/10.1016/0167-2738\(83\)90025-5](https://doi.org/10.1016/0167-2738(83)90025-5).
- [71] Y. Yuan and J. Huang, "Ion Migration in Organometal Trihalide Perovskite and Its Impact on Photovoltaic Efficiency and Stability," *Accounts of Chemical Research*, vol. 49, no. 2, pp. 286-293, 2016/02/16 2016, doi: 10.1021/acs.accounts.5b00420.
- [72] A. K. Jena, M. Ikegami, and T. Miyasaka, "Severe Morphological Deformation of Spiro-OMeTAD in (CH₃NH₃)PbI₃ Solar Cells at High Temperature," *ACS Energy Letters*, vol. 2, no. 8, pp. 1760-1761, 2017/08/11 2017, doi: 10.1021/acsenergylett.7b00582.
- [73] Y. Zhao *et al.*, "Mobile-Ion-Induced Degradation of Organic Hole-Selective Layers in Perovskite Solar Cells," *The Journal of Physical Chemistry C*, vol. 121, no. 27, pp. 14517-14523, 2017/07/13 2017, doi: 10.1021/acs.jpcc.7b04684.
- [74] M. Wang, H. Wang, W. Li, X. Hu, K. Sun, and Z. Zang, "Defect passivation using ultrathin PTAA layers for efficient and stable perovskite solar cells with a high fill factor and eliminated hysteresis," *Journal of Materials Chemistry A*, 10.1039/C9TA08314F vol. 7, no. 46, pp. 26421-26428, 2019, doi: 10.1039/C9TA08314F.
- [75] E. H. Jung *et al.*, "Efficient, stable and scalable perovskite solar cells using poly(3-hexylthiophene)," *Nature*, vol. 567, no. 7749, pp. 511-515, 2019/03/01 2019, doi: 10.1038/s41586-019-1036-3.
- [76] Y. Liu *et al.*, "High Efficiency and Stability of Inverted Perovskite Solar Cells Using Phenethyl Ammonium Iodide-Modified Interface of NiOx and Perovskite Layers," *ACS Applied Materials & Interfaces*, vol. 12, no. 1, pp. 771-779, 2020/01/08 2020, doi: 10.1021/acsaami.9b18217.
- [77] J. Cao, J. Yin, S. Yuan, Y. Zhao, J. Li, and N. Zheng, "Thiols as interfacial modifiers to enhance the performance and stability of perovskite solar cells," *Nanoscale*, 10.1039/C5NR01820J vol. 7, no. 21, pp. 9443-9447, 2015, doi: 10.1039/C5NR01820J.

- [78] T. S. Sherkar, C. Momblona, L. Gil-Escrig, H. J. Bolink, and L. J. A. Koster, "Improving Perovskite Solar Cells: Insights From a Validated Device Model," *Advanced Energy Materials*, vol. 7, no. 13, p. 1602432, 2017, doi: <https://doi.org/10.1002/aenm.201602432>.
- [79] C. Wang *et al.*, "Improving Performance and Stability of Planar Perovskite Solar Cells through Grain Boundary Passivation with Block Copolymers," *Solar RRL*, vol. 3, no. 9, p. 1900078, 2019, doi: <https://doi.org/10.1002/solr.201900078>.
- [80] H.-S. Kim and N.-G. Park, "Importance of tailoring lattice strain in halide perovskite crystals," *NPG Asia Materials*, vol. 12, no. 1, p. 78, 2020/12/11 2020, doi: 10.1038/s41427-020-00265-w.
- [81] B. Yang *et al.*, "Strain effects on halide perovskite solar cells," (in eng), *Chem Soc Rev*, vol. 51, no. 17, pp. 7509-7530, Aug 30 2022, doi: 10.1039/d2cs00278g.
- [82] B. Du, K. He, X. Zhao, and B. Li, "Defect Passivation Scheme toward High-Performance Halide Perovskite Solar Cells," *Polymers*, vol. 15, no. 9, p. 2010, 2023. [Online]. Available: <https://www.mdpi.com/2073-4360/15/9/2010>.
- [83] P. Su *et al.*, "Multifunctional and multi-site interfacial buffer layer for efficient and stable perovskite solar cells," *Chemical Engineering Journal*, vol. 472, p. 145077, 2023/09/15/ 2023, doi: <https://doi.org/10.1016/j.cej.2023.145077>.
- [84] Z. Zheng *et al.*, "Pre-Buried Additive for Cross-Layer Modification in Flexible Perovskite Solar Cells with Efficiency Exceeding 22%," *Advanced Materials*, vol. 34, no. 21, p. 2109879, 2022, doi: <https://doi.org/10.1002/adma.202109879>.
- [85] Q. Zhou *et al.*, "Revealing Steric-Hindrance-Dependent Buried Interface Defect Passivation Mechanism in Efficient and Stable Perovskite Solar Cells with Mitigated Tensile Stress," *Advanced Functional Materials*, vol. 32, no. 36, p. 2205507, 2022, doi: <https://doi.org/10.1002/adfm.202205507>.
- [86] Z. Weihao *et al.* *Perovskite Surface Passivation Using Thiophene-Based Small Molecules for Efficient and Stable Solar Cells*, doi: 10.1021/acsam.3c00549.s001.
- [87] C. Ni *et al.*, "Thiophene Cation Intercalation to Improve Band-Edge Integrity in Reduced-Dimensional Perovskites," *Angewandte Chemie International Edition*, vol. 59, no. 33, pp. 13977-13983, 2020, doi: <https://doi.org/10.1002/anie.202006112>.
- [88] U. Gunes *et al.*, "A Thienothiophene-Based Cation Treatment Allows Semitransparent Perovskite Solar Cells with Improved Efficiency and Stability," *Advanced Functional Materials*, vol. 31, 06/26 2021, doi: 10.1002/adfm.202103130.
- [89] M. Kundar *et al.*, "Surface Passivation by Sulfur-Based 2D (TEA)2PbI4 for Stable and Efficient Perovskite Solar Cells," *ACS Omega*, vol. 8, no. 14, pp. 12842-12852, 2023/04/11 2023, doi: 10.1021/acsomega.2c08126.
- [90] H. Zhen *et al.* *Mechanism of Enhancement in Perovskite Solar Cells by Organosulfur Amine Constructed 2D/3D Heterojunctions*, doi: 10.1021/acs.jpcc.1c04343.s001.
- [91] Y. Ma *et al.*, "Internal Interactions between Mixed Bulky Organic Cations on Passivating Defects in Perovskite Solar Cells," *ACS Applied Materials & Interfaces*, vol. 14, no. 9, pp. 11200-11210, 2022/03/09 2022, doi: 10.1021/acsami.1c18520.

- [92] E. R.-G. Carlo Andrea Riccardo Perini , Magdalena Rovello ,Andres Felipe Castro Mendez ,Juanita Hidalgo ,Yu An ,Ruipeng Li ,Carlos Silva-Acuña ,Juan-Pablo Correa-Baena "Preventing bulky cation diffusion in lead halide perovskite solar cells," *ChemRxiv* , 2021.
- [93] Y. Gao *et al.*, "Molecular engineering of organic-inorganic hybrid perovskites quantum wells," (in eng), *Nat Chem*, vol. 11, no. 12, pp. 1151-1157, Dec 2019, doi: 10.1038/s41557-019-0354-2.
- [94] H. C. Swart, "Surface Sensitive Techniques for Advanced Characterization of Luminescent Materials," (in eng), *Materials (Basel)*, vol. 10, no. 8, Aug 4 2017, doi: 10.3390/ma10080906.
- [95] S. Wiegold *et al.*, "Halide Heterogeneity Affects Local Charge Carrier Dynamics in Mixed-Ion Lead Perovskite Thin Films," *Chemistry of Materials*, vol. 31, 04/29 2019, doi: 10.1021/acs.chemmater.9b00650.
- [96] Z. Zhang and J. T. Yates, Jr., "Band Bending in Semiconductors: Chemical and Physical Consequences at Surfaces and Interfaces," *Chemical Reviews*, vol. 112, no. 10, pp. 5520-5551, 2012/10/10 2012, doi: 10.1021/cr3000626.
- [97] D. Sivadas, A. Singareddy, C. G. Vinod, and P. R. Nair, "Ionic Charge Imbalance in Perovskite Solar Cells," *The Journal of Physical Chemistry C*, 2023/11/13 2023, doi: 10.1021/acs.jpcc.3c05673.
- [98] C. Ma, D. Shen, T.-W. Ng, M.-F. Lo, and C.-S. Lee, "2D Perovskites with Short Interlayer Distance for High-Performance Solar Cell Application," *Advanced Materials*, vol. 30, no. 22, p. 1800710, 2018, doi: <https://doi.org/10.1002/adma.201800710>.
- [99] P. Chen, Y. Bai, S. Wang, M. Lyu, J. H. Yun, and L. Wang, "In Situ Growth of 2D Perovskite Capping Layer for Stable and Efficient Perovskite Solar Cells," *Advanced Functional Materials*, Article vol. 28, no. 17, 2018, Art no. 1706923, doi: 10.1002/adfm.201706923.
- [100] J. Hu *et al.*, "Synthetic control over orientational degeneracy of spacer cations enhances solar cell efficiency in two-dimensional perovskites," *Nature Communications*, vol. 10, no. 1, p. 1276, 2019/03/20 2019, doi: 10.1038/s41467-019-08980-x.
- [101] C. Katan, N. Mercier, and J. Even, "Quantum and Dielectric Confinement Effects in Lower-Dimensional Hybrid Perovskite Semiconductors," *Chemical Reviews*, vol. 119, no. 5, pp. 3140-3192, 2019/03/13 2019, doi: 10.1021/acs.chemrev.8b00417.
- [102] X. Wang, Y. Wang, T. Zhang, X. Liu, and Y. Zhao, "Steric Mixed-Cation 2D Perovskite as a Methylammonium Locker to Stabilize MAPbI₃," *Angewandte Chemie International Edition*, vol. 59, no. 4, pp. 1469-1473, 2020, doi: <https://doi.org/10.1002/anie.201911518>.
- [103] T. Wu *et al.*, "Efficient and Stable CsPbI₃ Solar Cells via Regulating Lattice Distortion with Surface Organic Terminal Groups," *Advanced Materials*, vol. 31, no. 24, p. 1900605, 2019, doi: <https://doi.org/10.1002/adma.201900605>.
- [104] Y. Yue *et al.*, "Peculiar Steric Hindrance Assists Monoclinic Phase Formation toward High-Quality All-Inorganic Perovskites," *The Journal of Physical Chemistry Letters*, vol. 12, no. 45, pp. 11228-11237, 2021/11/18 2021, doi: 10.1021/acs.jpcclett.1c03021.

- [105] H. B. Lee, N. Kumar, B. Tyagi, S. He, R. Sahani, and J. W. Kang, "Bulky organic cations engineered lead-halide perovskites: a review on dimensionality and optoelectronic applications," *Materials Today Energy*, vol. 21, p. 100759, 2021/09/01/ 2021, doi: <https://doi.org/10.1016/j.mtener.2021.100759>.
- [106] J. Hidalgo *et al.*, "Bulky cation hinders undesired secondary phases in FAPbI₃ perovskite solar cells," *Materials Today*, vol. 68, 07/01 2023, doi: 10.1016/j.mattod.2023.06.010.
- [107] R. Stanton and D. J. Trivedi, "Pyrovskite: A software package for the high-throughput construction, analysis, and featurization of two- and three-dimensional perovskite systems," *The Journal of Chemical Physics*, vol. 159, no. 6, 2023, doi: 10.1063/5.0159407.
- [108] C. Zhou *et al.*, "Low dimensional metal halide perovskites and hybrids," *Materials Science and Engineering: R: Reports*, vol. 137, pp. 38-65, 2019/07/01/ 2019, doi: <https://doi.org/10.1016/j.mser.2018.12.001>.
- [109] A. Z. Chen *et al.*, "Origin of vertical orientation in two-dimensional metal halide perovskites and its effect on photovoltaic performance," *Nature Communications*, vol. 9, no. 1, p. 1336, 2018/04/06 2018, doi: 10.1038/s41467-018-03757-0.
- [110] L. Gao *et al.*, "Improving charge transport via intermediate-controlled crystal growth in 2D perovskite solar cells," *Advanced Functional Materials*, vol. 29, no. 47, p. 1901652, 2019.
- [111] T. M. Koh *et al.*, "Nanostructuring Mixed-Dimensional Perovskites: A Route Toward Tunable, Efficient Photovoltaics," *Advanced Materials*, vol. 28, no. 19, pp. 3653-3661, 2016, doi: <https://doi.org/10.1002/adma.201506141>.
- [112] A. Amat *et al.*, "Cation-Induced Band-Gap Tuning in Organohalide Perovskites: Interplay of Spin–Orbit Coupling and Octahedra Tilting," *Nano Letters*, vol. 14, no. 6, pp. 3608-3616, 2014/06/11 2014, doi: 10.1021/nl5012992.
- [113] M. K. Jana *et al.*, "Direct-Bandgap 2D Silver–Bismuth Iodide Double Perovskite: The Structure-Directing Influence of an Oligothiophene Spacer Cation," *Journal of the American Chemical Society*, vol. 141, no. 19, pp. 7955-7964, 2019/05/15 2019, doi: 10.1021/jacs.9b02909.
- [114] K. Ma *et al.*, "Multifunctional Conjugated Ligand Engineering for Stable and Efficient Perovskite Solar Cells," *Advanced Materials*, vol. 33, no. 32, p. 2100791, 2021, doi: <https://doi.org/10.1002/adma.202100791>.
- [115] Y. Wu, J. Feng, Z. Yang, Y. Liu, and S. Liu, "Halide Perovskite: A Promising Candidate for Next-Generation X-Ray Detectors," *Advanced Science*, vol. 10, no. 1, p. 2205536, 2023, doi: <https://doi.org/10.1002/advs.202205536>.
- [116] X.-H. Zhu *et al.*, "Effect of Mono- versus Di-ammonium Cation of 2,2'-Bithiophene Derivatives on the Structure of Organic–Inorganic Hybrid Materials Based on Iodo Metallates," *Inorganic Chemistry*, vol. 42, no. 17, pp. 5330-5339, 2003/08/01 2003, doi: 10.1021/ic034235y.
- [117] D. B. Mitzi, K. Chondroudis, and C. R. Kagan, "Design, Structure, and Optical Properties of Organic–Inorganic Perovskites Containing an Oligothiophene Chromophore,"

- Inorganic Chemistry*, vol. 38, no. 26, pp. 6246-6256, 1999/12/01 1999, doi: 10.1021/ic991048k.
- [118] C. C. Stoumpos *et al.*, "Ruddlesden–Popper Hybrid Lead Iodide Perovskite 2D Homologous Semiconductors," *Chemistry of Materials*, vol. 28, no. 8, pp. 2852-2867, 2016/04/26 2016, doi: 10.1021/acs.chemmater.6b00847.
- [119] X. Zhang *et al.*, "Orientation regulation of phenylethylammonium cation based 2D perovskite solar cell with efficiency higher than 11%," *Advanced Energy Materials*, vol. 8, no. 14, p. 1702498, 2018.
- [120] J. Cho, J. DuBose, A. Le, and P. Kamat, "Suppressed Halide Ion Migration in 2D Lead Halide Perovskites," *ACS Materials Letters*, vol. XXXX, 04/21 2020, doi: 10.1021/acsmaterialslett.0c00124.
- [121] D. Meggiolaro, E. Mosconi, and F. Angelis, "Formation of Surface Defects Dominates Ion Migration in Lead-Halide Perovskites," *ACS Energy Letters*, vol. 4, 02/20 2019, doi: 10.1021/acseenergylett.9b00247.
- [122] S. Lee *et al.*, "Amine-Based Passivating Materials for Enhanced Optical Properties and Performance of Organic–Inorganic Perovskites in Light-Emitting Diodes," *The Journal of Physical Chemistry Letters*, vol. 8, no. 8, pp. 1784-1792, 2017/04/20 2017, doi: 10.1021/acs.jpcclett.7b00372.
- [123] C. Liu *et al.*, "Bimolecularly passivated interface enables efficient and stable inverted perovskite solar cells," *Science*, vol. 382, no. 6672, pp. 810-815, 2023, doi: doi:10.1126/science.adk1633.
- [124] H. Chen *et al.*, "Regulating surface potential maximizes voltage in all-perovskite tandems," *Nature*, vol. 613, no. 7945, pp. 676-681, 2023/01/01 2023, doi: 10.1038/s41586-022-05541-z.
- [125] P.-R. Yan, W.-J. Huang, and S.-H. Yang, "Incorporation of quaternary ammonium salts containing different counterions to improve the performance of inverted perovskite solar cells," *Chemical Physics Letters*, vol. 669, pp. 143-149, 2017/02/01/ 2017, doi: <https://doi.org/10.1016/j.cplett.2016.12.036>.